Ormaetxea Orobengoa, Joseba M.; Torres Canals, Francesc , dir. Sustainable energy storage devices using laser-induced graphene electrodes. 2021. (983 Grau en Nanociència i Nanotecnologia)

Sustainable energy storage devices using laser-induced graphene electrodes

Final Degree Project

Author:
Joseba M. Ormaetxea Orobengoa

UAB Supervisor:
Dr. Francesc Torres Canals

Institute Supervisors:
Marina Navarro Segarra
Dr. Juan Pablo Esquivel Bojorquez

Bachelor's degree in Nanoscience and Nanotechnology
Faculty of Sciences

Institut de Microelectrònica de Barcelona, IMB-CNM (CSIC)

Self-Powered Engineered Devices group (SPEED)

June 15, 2021

ABSTRACT

This project presents the development of laser-induced graphene (LIG) electrodes for application on sustainable electrochemical energy storage devices. Cardboard is selected as organic recyclable substrate, upon which fire-retardant treatments and lignin coatings have been tested prior to laser scribing. Laser conditions optimization have provided a cardboard derived conductor material with sheet resistance (R_s) values in the order of tens of $\Omega\cdot sq^{-1}$. Particularly, a newly developed lignin and nanocellulose coating treatment of cardboard has yielded 8.1 $\Omega\cdot sq^{-1}$ R_s, close to the best value reported for LIG on an organic substrate. Electrochemical and morphological characterization of cardboard based LIG showed that it presents a highly porous 3D electroactive surface. This material has been implemented in the fabrication of cardboard derived supercapacitors (SC) and batteries. Compared with polyimide derived LIG, cardboard SCs demonstrate higher areal capacitance (1 $mF\cdot cm^{-2}$), with similar performance to literature references. On the other hand, the biopolymer-based cardboard battery is the first proof-of-concept of its kind ever reported. Although it presents high internal resistance, the battery provides almost 1 V open circuit voltage, and a maximum power density output of 19.5 $\mu W\cdot cm^{-2}$. Thus, this work opens a new pathway in the research of potentially recyclable, biodegradable or even compostable batteries based on cardboard derived laser-induced graphene electrodes.

Keywords: *Laser-induced graphene, Cardboard, Energy storage devices, Supercapacitor, Battery*

ACKNOWLEDGEMENTS

First of all, I would like to personally show my gratitude towards Marina Navarro and Dr. Juan Pablo Esquivel, who have been my masters and references during my stay in the SPEED group. I owe them every grasp of second I have shared with them, for all the knowledge and positive energy they irradiate to those around them. I also thank all the wonderful people I have met as colleagues in the SPEED group and in IMB-CNM, because of all we have shared and everything they have taught me. All of you have made an unforgettable experience out of these months, and you are the main reason why I have always enjoyed it so much. Particularly, I express my thanks to David Batet for his help in SEM imaging, and Anna Llorella for his essential knowledge on supercapacitors. Finally, I would like to thank Universitat Autònoma de Barcelona and Institut de Microelectrònica de Barcelona for giving me the opportunity to experience such a wonderful stay in an outstanding research centre. And of course, this passage must end mentioning my family and friends, who I will always thank for being there, whatever I need, whenever.

CONTENTS

LIST OF FIGURES AND TABLES

- ***Figure 17.*** *a) Rs,parallel of LIG in different substrates, treatments, and conditions. b) Rs,perpendicular of LIG in different substrates, treatments, and conditions. N=4 4x4 mm^2 squares in each substrate, treatment and condition with discarded samples crossed out: c) PI_LIG_S9P9 d) FRS_LIG_S9P11_3mm e) FRS_LIG_S10P11_3mm f) FG_LIG_S8P11_3mm g) FG_LIG_S9P11_3mm h) LIGNIN+NC_LIG_S8P11 i) LIGNIN+NC_LIG_S10P12.*
- ***Figure 18.*** *CVs at different scan rates. a) In PI_LIG_S9P9 electrodes. b) In FRS_LIG_S9P11_3mm electrodes.*
- ***Table 1.*** *ECSA/GA ratios and k° for different electrode types.*
- ***Figure 19.*** *SEM images of sample surfaces: a) and b) FG_LIG_S9P11_3mm. c) LIGNIN+NC_LIG_S10P12. d) LIGNIN+NC_LIG_S8P11. e) PI_LIG_S9P9. Cross section: f) FG_LIG_S8P11_3mm.*
- ***Table 2.*** *Thickness of produced LIG in different substrates.*
- ***Figure 20.*** *CVs at different scan rates. a) For SCs based on PI. b) For SCs based on cardboard.*
- ***Table 3.*** *Areal capacitance (in mF·cm^{-2}) calculated from CVs with equation (6).*
- ***Figure 21.*** *a) GCDs for SCs based on PI at 5 µA. b) GCDs for SCs based on cardboard at 20 µA.*
- ***Table 4.*** *Figures calculated from GCD experiments.*
- ***Figure 22.*** *a) OCVs for manufactured batteries, with pressure applied. b) LSV and power output characteristic for battery based on Kapton and power output. c) LSV and power output characteristic for battery based on cardboard.*
- ***Table 5.*** *Figures calculated for PI and cardboard based batteries.*
- ***Figure 23.*** *Schematic concept illustration showing the cyclic process for the development of sustainable energy storage devices using LIG electrodes.*
- ***Figure 24.*** *Cardboard rastered with the same lasing parameters at different positions of the sample stage. a) with extractor switched on, and b) with extractor switched off (scalebar for sample stage, 90 mm; squares in insight pictures are 4x4 mm^2 sized).*
- ***Figure 25.*** *Variation of lased spot separation with DPI resolution and defocus. a) In X axis. b) In Y axis. c) Variation of lased spot diameter with DPI resolution and defocus.*
- ***Figure 26.*** *a) CVs performed in LIGNIN+NC_LIG electrodes with varying scan rate with 100 mM ferricyanide and 1M KCl. LIGNIN+NC membrane mechanical destabilization in DI water. b) Seconds after immersion. c) One hour after immersion. d) After removing membrane from water it broke.*
- ***Figure 27.*** *a) Optical microscope image of interdigitated electrodes of FRS_SC with corel design superimposed in yellow. d) Optical microscope image of interdigitated electrodes of PI_SC with Corel design superimposed in yellow.*
- ***Figure 28.*** *Different lignin treatments tested on cardboard a) Bar coating of hydrogel (scalebar, 1 cm). b) Water evaporation of hydrogel on Petri dish (scalebar, 1 cm). c) Lignin aqueous solution spraying (scalebar, 4 cm).*
- ***Figure 29.*** *CVs performed with fire-retardant treated cardboard derived LIG electrodes vs SPE, in 100 mM ferricyanide 1 M KCl solution, with a commercial Ag/AgCl reference electrode and a Pt counter electrode, at 20 mV·s^{-1} scan rate. a) FRS_LIG_S9P11_3mm electrodes. b) FRS_LIG_S10P11_3mm electrodes. c) FG_LIG_S8P11_3mm electrodes. d) FG_LIG_S9P11_3mm electrodes.*
- ***Figure 30.*** *Microscope images showing trench in the border of scribed FG treated cardboard, disabling it for interdigitated electrode fabrication. a) 4x4 mm^2 square of FG_LIG_S8P11_3mm in the four-point probe station (scalebar, 1 mm). b) Scanning electron microscope image (1 kV) of 4x4 mm^2 square border, showing a deep trench. c) Optical microscope image of interdigitated electrodes fabricated with FG_LIG, showing structures with several defects and very narrow LIG conductor path.*

LIST OF ABBREVIATIONS

GHG	GreenHouse Gas
EES	Electrochemical Energy Storage
EDLC	Electrical Double-Layer Capacitor
ULAB	Used Lead-Acid Battery
LIG	Laser-Induced Graphene
PI	PolyImide
GO	Graphene Oxide
SEM	Scanning Electron Microscopy
TEM	Transmission Electron Microscopy
CSIC	Consejo Superior de Investigaciones Científicas
IMB-CNM	Institut de Microelectrònica de Barcelona – Centre Nacional de Microelectrònica
SPEED	Self-Power EnginEered Devices
R_s	Sheet Resistance
$R_{s,parallel}$	Sheet Resistance Parallel to laser raster direction
$R_{s,perpendicular}$	Sheet Resistance Perpendicular to laser raster direction
CV	Cyclic Voltammetry
RE	Reference Electrode
WE	Working Electrode
CE	Counter Electrode
ECSA	ElectroChemically active Surface Area
SC	SuperCapacitor
GCD	Galvanostatic Charge-Discharge
C_A	Areal Capacitance
CE	Coulombic Efficiency
EE	Energy Efficiency
OCV	Open Circuit Voltage
LSV	Linear Sweep Voltammetry
FRS	Flame Retardant Spray
FG	FireGuard
CMC	CarboxyMethylCellulose
DI	DeIonized
NC	NanoCellulose
S	Speed
P	Power
SPE	Screen-Printed Electrode
GA	Geometrical Area
CNT	Carbon NanoTube

1. INTRODUCTION

1.1. CONTEXT

Nowadays, there is a general scientific consensus that human activity is affecting global climate, and it has become a growing concern in society.[1] Climate change has been known since long ago, as in 1896 Arrhenius himself demonstrated that CO_2 produced in fossil fuel burning could warm the Earth.[2] Little was done in order to tackle this problem through the XXth century, but new environmental policies have recently emerged to reduce greenhouse gas (GHG) emissions. For instance, the Paris Agreement was signed in 2015, where governments agreed to strengthen the global response to climate change.[3] A 2°C limit was set to the increase in Earth's average temperature compared with pre-industrial levels. However, human activities have caused a 1°C raise so far. It is estimated to reach 1.5°C by 2050 if current emission rates stand.[4] Therefore, a global energy transition towards decarbonisation is necessary to reduce dependence on fossil fuels and accomplish the objectives pursued.[5]

As a means to stabilize the atmospheric carbon content, renewable energy sources that minimize GHG emissions are gaining interest. Besides decarbonisation of energy production, improving the distribution, storage, and conversion efficiencies[6] is fundamental. In fact, the main challenge of most renewable sources is their intrinsic intermittency. Consequently, energy storage systems are needed to ensure grid stability and reliability. Many technologies have been developed to face this challenge, ranging from hydroelectric and thermal to hydrogen and electrochemical storage.[7,8] All of them include pros and cons, and an integrated combination is probably the best solution to satisfy the demand.[9]

Electrochemical energy storage (EES) consists in conversion between electrical and chemical energy, allowing its storage, transport, and supply on demand. There are four main EES systems: batteries, fuel cells, redox-flow cells, and supercapacitors.[10] As for batteries, two types are differentiated: primary batteries are single use, whereas secondary ones are rechargeable. In electrochemical capacitors, also named supercapacitors, there are two main types: electrical double layer capacitors (EDLC) and pseudocapacitors.[11] EES systems present flexible power and capacity characteristics, as well as size scalability to fulfil different portability requirements.[8,10] Despite the great progress in performance over the years, the current production of EES systems still follows a linear model, starting from fabrication with scarce non-renewable materials, followed by distribution, consumption and disposing of, thus contributing to environment degradation.[12]

ENVIRONMENTAL CONSIDERATIONS OF PRIMARY BATTERIES

Out of the 191 kilotons of portable batteries sold in Europe in 2018, 75% corresponded to primary type.[13,14] These devices contain hazardous compounds, such as heavy metals and metal oxides that harm ecosystems in case of leakage during their operational lifespan or improper management at the end of it.[15] Batteries can follow different paths after their use, such as landfilling or recycling by thermal, mechanical and manual treatments.[16] To avoid the risks of contamination, it is important to develop efficient recovery and recycling protocols. In the same year, 52% of portable batteries sold in the EU were lost in waste, most of them ending up in landfills, poisoning ecosystem.[13,15] Current recycling techniques of metals, for instance, present some drawbacks, such as high economic cost and energy consumption or toxic off-gas and dust by-product generation.[17] Moreover, batteries often travel thousands of kilometres to countries where they are treated in precarious conditions. For example, the World Health Organization and United Nations Environment Programme have reported the existence of numerous informal used lead-acid battery (ULAB) sites in developing countries, as well as their hazard for human health and environment.[18,19]

Consequently, recent research tries to develop more environmentally friendly and safer battery technologies.[20,21] Among other innovations, new electrode materials are being investigated.[22] Traditionally, transition metal and metal-oxides have been used as electrode materials.[23] Noble metals, such as Pt and Pd, have also been employed as current collectors or catalysts, but these are generally expensive and scarce.[24] Al and Cu are also common, but they have parasitic reaction problems and their recyclability is still controversial.[25] In contrast, metal-free carbon-based current-collectors can provide some advantages, like low-cost, abundant availability (can even be extracted from biomass) and non-toxicity.[26] Moreover, they present proper performance characteristics: high electric conductivity, electrochemical stability (very inert) and fast electronic transference.[27] In this context, graphene stands out thanks to its great electric conductivity, large surface area and electro-catalytic activity.[28] It has already been tested in EES devices[29] and emerges as a promising candidate to overthrow conventional metallic electrodes. However, graphene is usually synthesized with high economic and energy cost.[30] An interesting solution recently discovered along this track is laser-induced graphene (LIG). This technique has attracted a lot of attention due to its low cost and simplicity to produce a material with graphene-related nature.

LASER-INDUCED GRAPHENE (LIG) - STATE OF THE ART

In 2014, J. Lin et al. discovered that direct lasing with a CO_2 infrared laser on a commercial polymer tape (Kapton polyimide, PI) can generate 3D porous graphene on the film (Figure 1a).[31]

It was later determined that both photochemical and photothermal processes take part in this reaction. The CO_2 laser outputs a 10.6 µm centred band, which is absorbed by C−C bonds present in the precursor substrate materials (Figure 1b).[32] This absorption creates localized high temperature and pressure, breaking C-O, C=O and N-C bonds. Carbon atoms rearrange to form 3D porous graphene.[33–35]

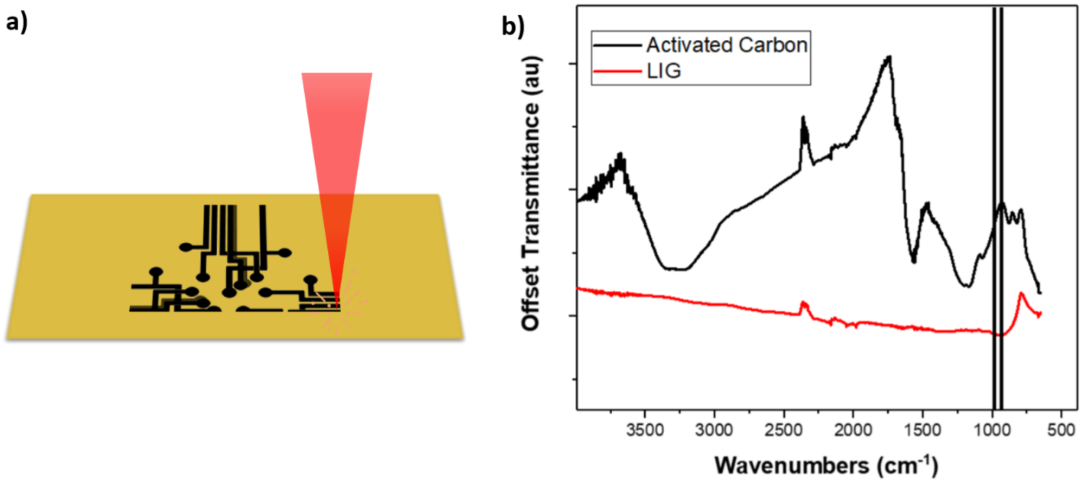

Figure 1. *a) Illustration of LIG technique on PI (elaborated by the author). b) Absorption spectrum of amorphous carbon and LIG, with CO_2 laser bands as vertical lines (Reprinted by permission from CCC RightsLink®: ACS Nano, Laser-Induced Graphene by Multiple Lasing: Toward Electronics on Cloth, Paper, and Food[36], Yieu Chyan, Ruquan Ye, Yilun Li, et al, Copyright © 2018, American Chemical Society).*

Laser-induced graphene technique is striking because it combines 3D graphene preparation and patterning into a single step.[37] It basically consists in laser scribing on PI under very specific conditions with a commercial CO_2 laser system. Until the discovery of LIG the most widely used fabrication techniques were chemical vapour deposition and hydrothermal processing. These require either high-temperature steps, long synthesis routes or high economic costs. Graphene patterning by hydrated graphene oxide (GO) laser writing is possible, but it is unappealing as GO is expensive and involves lots of acidic and oxidizing waste.[37] Thus, LIG stands out as a promising choice against its direct competition to produce 3D porous graphene. This material presents a high surface area together with the remarkable chemical, physical and electronic attributes of graphene.[38]

Regarding the substrate, later studies have shown that PI is not the only possible precursor for LIG. Laser-induced graphene has been produced on many other organic substrates so far. Biobased precursors include cellulose nanofiber,[39] wood[40] and lignin.[40–43] J. M. Tour et al.[32] tested cork, coconut, potato skin, bread, cotton paper, cardboard and cloth. Several plastic polymers (Kevlar, PEI, PSU…) have also been used with success.[34] Resulting qualities partially depend on the starting material.[32,39,40,42,43] For example, in lignocellulosic biomaterials a higher lignin content over cellulose and hemicellulose generates less defects on the obtained graphene.[40]

As previously stated, LIG generation requires specific laser conditions for each substrate, which must be optimized. These include lasing power and speed (and, consequently, exposition time),[43–45] light wavelength,[46] atmosphere composition,[47] number of lasing steps,[36,44,45] and defocusing.[36,45] When it comes to power and speed, they determine the energy absorbed by the lased atoms: higher power and lower speed result in more energy absorbed per unit area. Then, incident photon flow rate is also crucial. For example, higher laser powers generate higher porosity and larger pore sizes, though there is an upper limit that causes structural failure if surpassed.[37] Increasing lasing steps can lead to LIG using milder speed-power conditions. In the first raster scan amorphous carbon is obtained, and subsequent scribing turns it into graphene. Varying the relative laser-substrate z-position causes defocusing, i.e. the diameter of the laser spot on the substrate is larger, resulting in decreased irradiance (incident power per unit area) and therefore achieving a similar effect to multiple lasing but in a single step (Figure 2).[36] Regarding working atmosphere, several composition changes have been tried to perform heteroatom doping on resulting 3D porous graphene.[37] The same effect can be achieved by putting additives to the initial substrate, such as boric acid to obtain B-LIG (boron doped).[48] These are in-situ modifications, but ex-situ modifications have also been reported, e.g. by surface treatment with an electrodeposition process.[49]

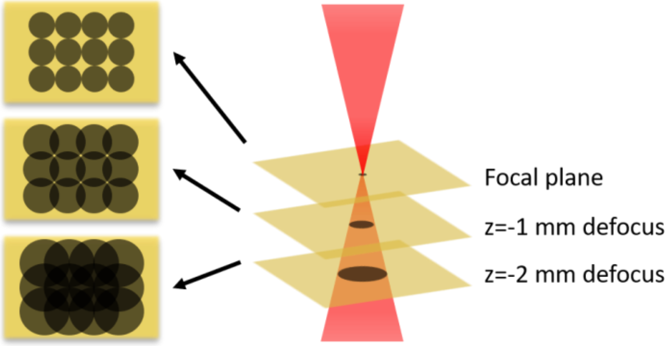

Figure 2. *Effect of defocus on raster laser scribing upon precursor (elaborated by the author).*

In conclusion, laser-induced graphene has been produced in a wide variety of methods, showing how different conditions affect the creation and quality of the obtained graphene. This has allowed to characterize the morphological, chemical, and electrical properties of LIG.[31,36,37,39,42,49–52] As for the morphological aspect, the surface appearance in scanning electron microscopy (SEM) images differs depending on the original substrate, but it generally presents highly amorphous and porous structures.[37] Depending on the lasing parameters, several shapes can be achieved, such as honeycomb networks, microporous foams, concave corrugated tiles and carbon nanotubes.[53] The graphene-related nature of LIG is clearly visible in transmission electron microscopy (TEM) images (Figure 3).[31]

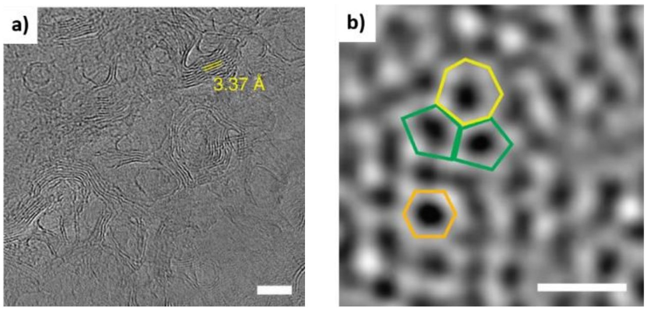

Figure 3. *a) High-resolution TEM image of LIG showing lattice space of 3.37 Å that corresponds to (002) graphitic planes (scale bar, 10 nm. b) Spherical aberration corrected scanning TEM image of LIG showing heptagon, pentagon and hexagon carbon cycles (scale bar, 5 Å) (Reprinted by permission from CCC RightsLink®: Nature Communications, Laser-induced porous graphene films from commercial polymers[31], Jian Lin et al, Copyright © 2014, Nature Publishing Group, a division of Macmillan Publishers Limited. All Rights Reserved).*

Regarding chemical characterization of LIG, two major spectroscopic techniques are used for its analysis. In X-ray photoelectron spectroscopy studies an increase in carbon and C-C bond content is observed in LIG compared to initial substrates.[31,36,39,42,49–51] Raman spectroscopy shows distinctive D (1350 cm^{-1}), G (1580 cm^{-1}) and 2D (2700 cm^{-1}) bands in LIG.[31,36,37,39,42,49,51,52] Concerning crystallographic structure, X-ray diffraction patterns exhibit an intense peak in $2\theta = 25.9°$ due to 3.4 Å spacing of (002) planes.[31] As for LIG's electric conductivity, it is generally assessed using a four-point probe station to extract its sheet-resistance value.[31,36,50,51] Among the literature, reported values range from 3.8 to 250 $\Omega\cdot sq^{-1}$. This wide variability in the results is attributed to the different factors influencing LIG's creation and quality, as mentioned above.

Taking advantage of the unique characteristics of this 3D porous graphene-based material many applications have been reported so far: supercapacitors,[31,48] heaters,[50] a HER and OER catalyser,[51] humidity sensors,[43] flexible electrodes for microfluidic devices,[54] magnetic hydrodynamic pumps,[55] sound and deformation detectors,[56,57] chemical sensors,[58] and photodetectors.[59] In combination with metallic catalysts (Pt, Co, Mn, Zn…), it has also been used for battery development, always using PI as precursor.[60–65] However, as for May 2021 no reference has been found where LIG alone has been employed as electrode in the development of biopolymer based batteries, or having cardboard as substrate precursor.

SPEED GROUP at IMB-CNM (CSIC)

In this context, the Self-Powered Engineered Devices (SPEED) group from Institut de Microelectrònica de Barcelona, IMB-CNM (CSIC) has identified LIG as a suitable electrode material for sustainable battery fabrication. The SPEED group, led by Dr. Juan Pablo Esquivel and Dr. Neus Sabaté, specializes on the development of disposable portable energy sources by integrating different technologies. The research team is renowned for devising a metal-free and biotically degradable battery (the PowerPAD),[66] and devices such as a self-powered glucometer[67] and a smart patch for sweat conductivity monitoring,[68] among many others. Taking into consideration the characteristics of laser-induced graphene, they already began its analysis on PI and organic substrates such as paper or cardboard, in previous Final Degree Projects from students of Universitat Autònoma de Barcelona.[44,45] In this line, the SPEED group aims to implement LIG in their future creations as a means to develop innovative batteries that contribute to change the current energy storage paradigm into more sustainable and eco-friendly pathways.

1.2. OBJECTIVES

The main goal of this Final Degree Project is the development of portable electrochemical power sources using LIG as current collector material. This work involves a thorough study of fabrication of LIG on different organic substrates, pre-treatments, and lasing scribing parameters, to obtain a recyclable, biodegradable, or even compostable electrode. LIG is characterized electrically, morphologically, and electrochemically to seek for the conditions that give the most suitable attributes for its applications. Finally, its integration in supercapacitors and batteries is investigated building prototypes and evaluating their performance.

In order to fulfil these aspirations, many complementary objectives are also aimed. These include learning to use instruments and techniques for fabrication, prototyping and characterization of materials and devices. Besides, daily laboratory procedures and safety measures will be practiced. As the project is carried out in a research group, soft skills such as teamworking and communication will be key in the working environment. Last, bibliography research and experimental data acquisition, analysis, organization, and exposition will be exercised. All of that will involve motivating autonomy and self-responsibility in the research centre.

2. THEORETICAL FRAMEWORK

2.1. LIG CHARACTERIZATION TECHNIQUES

ELECTRICAL RESISTANCE CHARACTERIZATION

The Van der Pauw method is used for sheet resistance (R_s) measurements.[69] A flat square sample of the studied material is contacted in its 4 vertices (Figure 4a). A current scan is forced through one edge while the voltage drop is being measured on the other. The R_s is calculated from the I-V slope applying eq. (1) (Figure 4b).[70]

$$I = V \cdot \frac{\pi}{\ln 2} R_s \qquad (1)$$

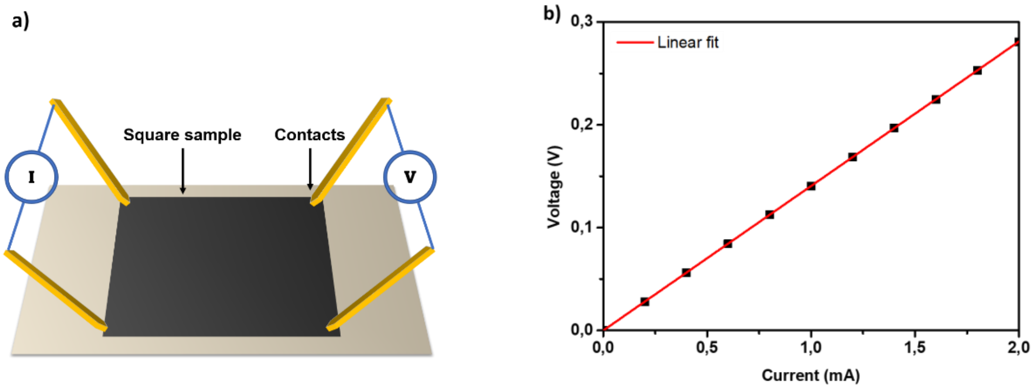

Figure 4. *a) Illustration of Van der Pauw method setup (elaborated by the author). b) I-V diagram obtained from Van der Pauw method experiment.*

ELECTROCHEMICAL CHARACTERIZATION

Cyclic voltammetry (CV) is a well-known electroanalytical technique employed to investigate redox reactions.[71] The experiment is performed in an electrochemical cell, typically a 3-electrode setup in contact with a solution (Figure 5a). The solution consists of a supporting electrolyte (i.e. an inert salt) and the redox species in an inert solvent. The reference electrode (RE) has a defined and stable equilibrium potential. It is used as a reference point against which the potential of the working electrode can be measured. The working electrode (WE) carries out the electrochemical event of interest. Finally, a counter electrode is used to compensate charge transfer. For instance, when an oxidation reaction is going on in the WE, a reduction reaction (or vice versa) takes place on this auxiliary electrode balancing the current flow.

In a CV the potential between RE and WE is scanned from a starting point through a pre-set range (Figure 5b). The redox species react on the surface of the WE to reach equilibrium concentrations that vary with voltage. The WE collects or provides electrons for the redox reactions and the current between WE and CE is recorded (Figure 5c). The output is a cyclic voltammogram with characteristic peaks that depend on the system (Figure 5d).

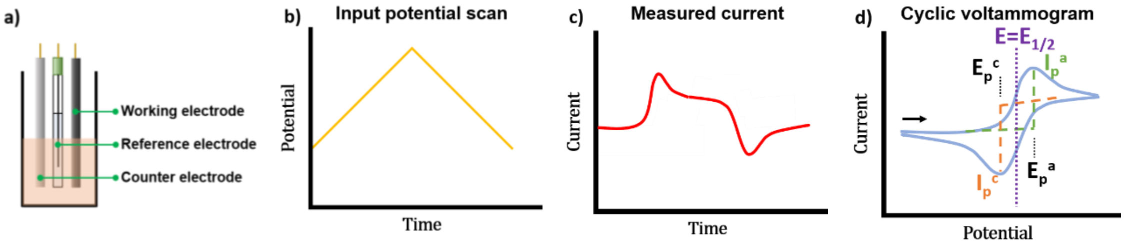

Figure 5. *a) Schematic representation of an electrochemical cell for CV experiments. b) WE vs RE potential evolution during a CV experiment. c) Current evolution during a CV experiment. d) Cyclic voltammogram with parameters that can be obtained (elaborated by the author).*

The Randles-Sevcik equation[72,73] (eq. 2) relates the peak current, i_p, with the scan rate v in reversible systems. n is the number of electrons transferred in the redox reaction, A the electrochemically active electrode surface area (ECSA), D the diffusion coefficient of the analyte, C^0 the bulk concentration of analyte, F Faraday's constant, T the temperature and R the molar gas constant. If the rest of parameters are known, the ECSA can be calculated from a voltammogram. When treating quasi-reversible systems, the above equation is slightly modified (eq. 3).[28] In reversible systems, reduction and oxidation peak intensity ratio is approximately 1. However, in quasi-reversible systems this ratio gets lower, as one of the peaks presents higher intensity than the other.

$$i_p = 0.446nFAC^0(\frac{nF\upsilon D}{RT})^{\frac{1}{2}} \tag{2}$$

$$i_p{}^{qr} = \pm(2.65 \times 10^5)n^{\frac{3}{2}}ACD^{\frac{1}{2}}\upsilon^{\frac{1}{2}} \tag{3}$$

On the other hand, in order to estimate the standard heterogeneous electron transfer rate constant (k^o, $cm \cdot s^{-1}$) Nicholson's method is applied in reversible systems (eq. 4).[28,74] Ψ is a kinetic parameter obtained from eq. (5),[75] where ΔE_p is potential difference between oxidation and reduction peaks. In quasi-reversible systems, eq. (6) is used, α being the transfer coefficient.[76]

$$\psi = k^o[\frac{\pi Dn\upsilon F}{RT}]^{-\frac{1}{2}} \tag{4}$$

$$\psi = \frac{-0.6288 + 0.021\Delta E_p}{1 - 0.017\Delta E_p} \tag{5}$$

$$k^o = 2.18[\frac{D\alpha n\upsilon F}{RT}]^{\frac{1}{2}} \exp[-\frac{\alpha^2 nF\Delta E_p}{RT}] \tag{6}$$

2.2. ELECTROCHEMICAL ENERGY STORAGE DEVICES

SUPERCAPACITORS

A classical capacitor is composed of two parallel conductor plates separated by a dielectric. Its operation principle consists in the accumulation of opposite charge when a potential difference is applied between the plates. Instead of a dielectric, a supercapacitor (SC) has an electrolyte in between, and two main types exist, electrical double layer capacitors (EDLC) and pseudocapacitors.[11] In EDLCs, apart from the charges accumulated in the conductors, electrolyte ions adsorb on their surface, forming a double electrical layer in each. In pseudocapacitors, aside from ion adsorption redox reactions provide charge on electrodes.

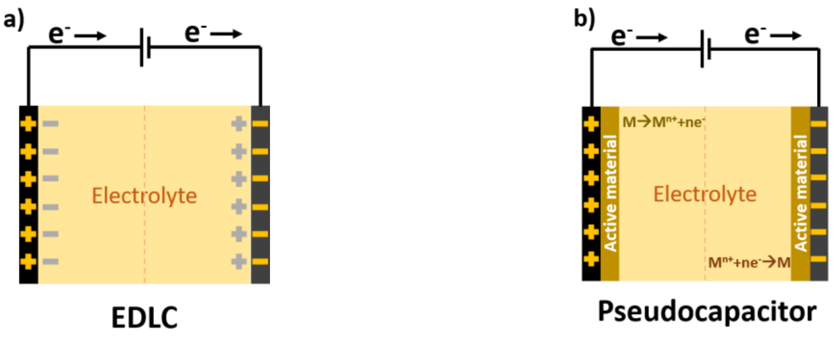

Figure 6. *a) Working mechanism of electric double layer capacitor. b) Working mechanism of pseudocapacitor (elaborated by the author).*

In general, capacitor electrodes can be made of three materials: carbon-based materials, metal transition oxides and conductive polymers. Further, there are three electrolyte types too: organic, ionic acid and aqueous. As for geometry, apart from the classical parallel plate capacitors, 2D interdigitated SCs are an appealing option for easy integration.

An ideal SC presents a square cyclic voltammogram, but output resistance and current leakage between electrodes can distort the diagram (Figure 7a-d).[78] One can integrate the area enclosed in the voltammogram to calculate the specific areal capacitance (C_A, in $F \cdot cm^{-2}$) of a SC (eq. 7),[79] taking into account the scan rate (v) and the area of electrodes (A).

Another standardized characterization technique is a galvanostatic charge-discharge (GCD) or chronopotentiometry experiment,[79] in which a constant current is applied across the device until a set voltage is obtained. The SC is discharged applying the opposite current. Potential evolution along time is plotted. Ideal capacitors, in which the charge and discharge pattern are mirror images, are characterized by a perfectly triangular curve (Figure 7e).[78,80] In this case, the discharge slope is used to calculate C_A (eq. 8).[78] However, asymmetry of the system, energy and charge loss, series resistance of the device and pseudocapacitive behaviour can cause deviations from this idea curve (Figure 7f), making capacitance dependent on voltage. In such devices, other characteristics may be analysed.[81] From GCD curves coulombic efficiency can be calculated as accumulated and released charge ratio (eq. 9). Similarly, energy efficiency is the analogous but with energies instead of charge, computing input and output energy with the area under the curve (eq. 10). Moreover, employing the discharge energy, system's effective areal capacitance can be calculated (eq. 11). Finally, equivalent series resistance can be calculated using V_{IR} voltage drop at beginning of discharge (eq. 12).

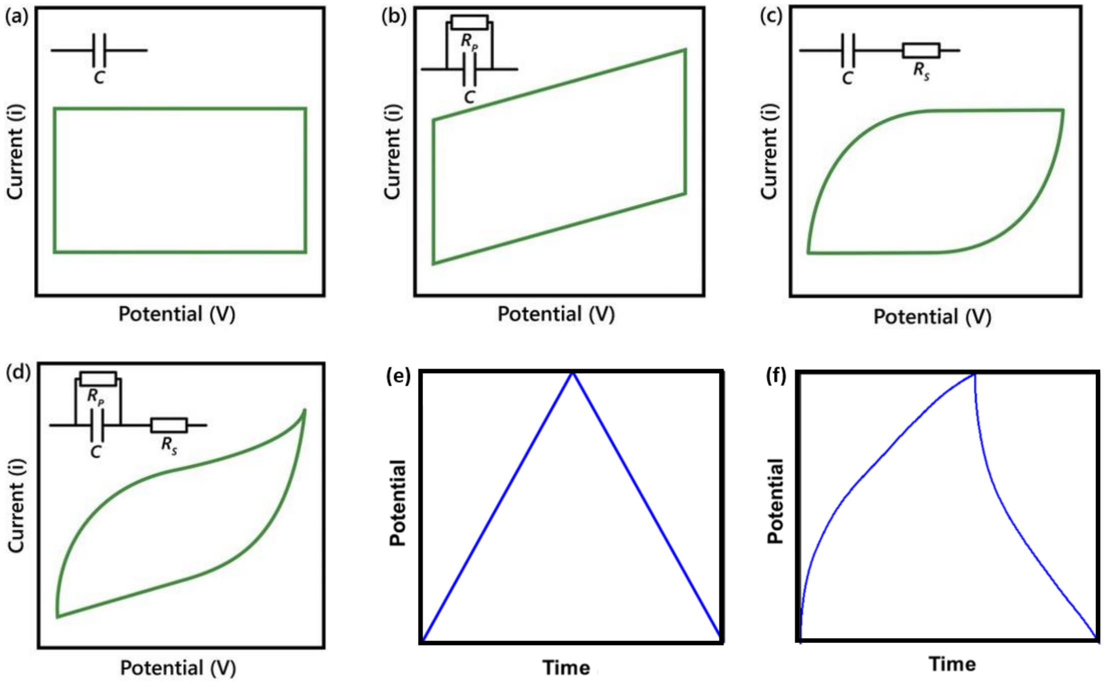

Figure 7. *Equivalent circuit analysis for different CV profiles. a) Ideal CV profile. b) Slanted. c) Blunt. d) Mix of blunt and slanted. (Reprinted by permission from CCC RightsLink®: Advanced Energy Materials, Energy Storage Data Reporting in Perspective—Guidelines for Interpreting the Performance of Electrochemical Energy Storage Systems[82], Yury Gogotsi, Patrice Simon, David Pinto, et al, Copyright © 2019 WILEY-VCH Verlag GmbH & Co. KGaA, Weinheim). Galvanostatic charge discharge curves. e) Ideal SC. f) Non-ideal SC. (Adapted by permission from CCC RightsLink®: Nano Energy, Flexible solid-state electrochemical supercapacitors[78], Peihua Yang,Wenjie Mai, Copyright © 2014 Elsevier Ltd. All rights reserved).*

$$C_A = \frac{\oint IdV}{2vA\Delta V} \tag{7}$$

$$C_A = \frac{I\Delta t}{A\Delta V} \tag{8}$$

$$CE = \frac{Q_{out}}{Q_{in}} = \frac{I_{discharge}t_{discharge}}{I_{charge}t_{charge}} \tag{9}$$

$$EE = \frac{E_{out}}{E_{in}} = \frac{I\int_{t(V_{max})}^{t(V_f)} Vdt}{I\int_{t(V_i)}^{t(V_{max})} Vdt} \tag{10}$$

$$C_{A,eff} = \frac{2E_{out}}{A\Delta V^2} \tag{11}$$

$$R_{se} = \frac{V_{IR}}{2I} \tag{12}$$

BATTERIES

A battery is a galvanic electrochemical cell that converts chemical energy directly to electrical energy via redox reactions.[83] Usually, it is composed of two electrodes: an anode in which the oxidation reaction takes places, and a cathode that balances the extracted electrons by a reduction reaction. Electrodes have different redox potentials so that a voltage difference is generated between them, named open circuit voltage (OCV). Both electrodes are ionically connected through a salt bridge or an ion exchange membrane, ensuring charge compensation.

Linear sweep voltammetry (LSV) is a technique employed in battery characterization. Electrodes are connected to a potentiostat and voltage is scanned from OCV to short circuit, as current is measured. Typical I-V polarization curves show an initial steep decrease due to activation losses, a constant slope related to ohmic losses and a final decrease due to mass transport loss at high current densities (Figure 8b).[84] Multiplying applied voltage and measured current the power output at each operating point is computed.

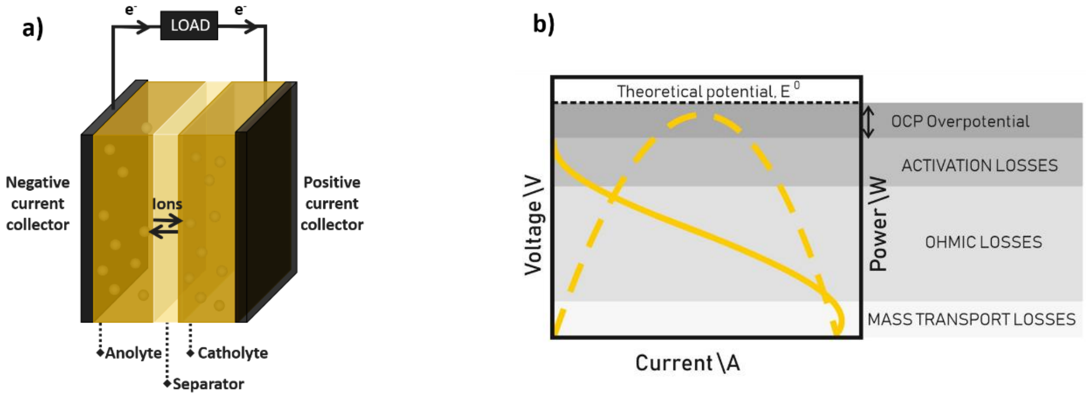

Figure 8. *a) Working mechanism of a battery. b) Polarization curve characteristics and power output (elaborated by the SPEED group).*

3. MATERIALS AND METHODS

3.1. SUBSTRATE

Cardboard was selected as organic substrate as it is the most used and recycled packaging material in EU.[85,86] LIG obtention on cardboard has already been successfully reported.[36,44] In this work, several cardboard samples were collected and their structural, mechanical, appearance and stability characteristics considered for the study. Corrugated type is undesirable as surface is heterogeneous because of slight ripples. In contrast, solid cardboards present flat homogeneous surfaces. Among different options, Buffetti MOD. 7759-K solid cardboard file folders were chosen. These are made of Manilla type cardboard, typically employed in file folders. As for structure, it is 370 µm thick and weights 250 $g \cdot m^{-2}$, with high fibre density. Mechanically, Manilla type is a relatively rigid and resilient solid cardboard, with 2650 m breaking length and 140 kPa bursting strength.[88] It presents high dimensional stability allowing surface treatments without compromising the substrate integrity. Furthermore, these folders are an abundant source of obsolete reusable material at IMB-CNM. They have different surfaces on the inside and outside, but the inner side was selected as it is less contaminated by past use.

Polyimide (PI, DuPont™ Kapton®) was chosen as reference material to produce LIG and compare performance, as its use is widely reported.[30]

As reported in the literature, the definition of LIG structures on cardboard requires the impregnation of the surface with a flame retardant. In this work, several pretreatments were tested. On the one hand, two commercial fire retardants already used in published reports were used: phosphate ammonium based ForceField® FireGuard for Fabrics (Shield Industries, Inc.) and boric acid based Flame Retardant Spray (FireChief®). Each product was applied separately by spraying 6 times on a 10x10 cm^2 square cardboard piece and dried overnight.

On the other hand, an alternative bio-based coating approach was proposed with two purposes, first, to act as a flame retardant with an eco-friendlier chemical composition; and second, to increase the lignin content on the substrate surface to improve LIG quality. In this approach, 4 impregnation methods were tested: spraying and painting with aqueous lignin solution, bar coating of lignin-hydrogels and membrane casting by evaporation of lignin-hydrogels.

The preparation of the aqueous lignin solution consisted in stirring 3 g lignin (Lignin alkali 471003 from Sigma-Aldrich) and deionized (DI) water for 10 minutes until homogenization. The resulting 3% w/v lignin in DI water dispersion was sprayed on cardboard or painted with a soaked paper. Lignin hydrogels combined with biopolymers were developed and applied in two ways: bar coating and membrane casting by evaporation. First, 1.5% w/v carboxymethylcellulose sodium salt hydrogels (CMC, GC7698 from Glentham Life Sciences) with different lignin contents (1%, 2% and 3% w/v) were prepared. 0.9 g CMC were stirred at 200 rpm overnight in 60 ml DI water before adding the lignin and further stirring at 200 rpm overnight. It was spread on cardboard with K Printing Proofer (RK Printcoat Instruments). Second, a 1% w/v nanocellulose (NC, Exilva P 01-V from Borregaard) hydrogel with 3% w/v lignin was tested. 5 g of 10% w/v NC were dispersed in 45 ml DI water at 10000 rpm for 5 minutes with T 25 digital ULTRA-TURRAX® (IKA-Werke). 1.5 g of lignin were added and stirred at 200 rpm for two hours. 20 ml of dispersion were poured on the cardboard over a Petri dish and let dry 72 hours at 25°C in an incubator (Hach Lange S.L.U. L2-01).

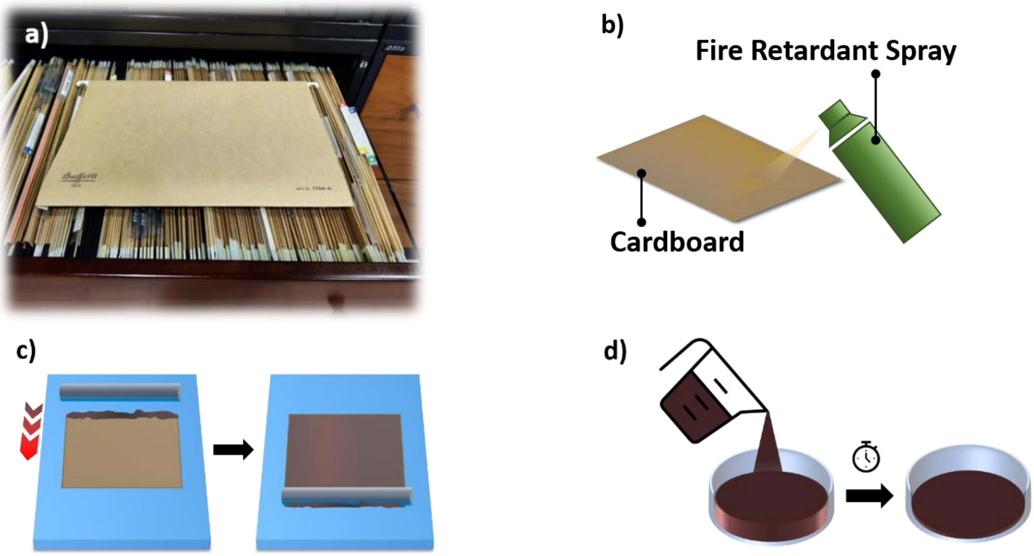

Figure 9. *a) Cardboard file folder from CNM obsolete filing cabinet. b) Illustration of fire-retardant treatment. c) Illustration of lignin treatment by bar coating d) Illustration of lignin treatment by water evaporation (elaborated by the author).*

3.2. LASING CONDITIONS OPTIMIZATION

Laser scribing was performed with an Epilog Legend Mini 24 instrument (Figure 10). It has a motorized mirror and lens system to direct the beam upon the substrate to cut or engrave it. Raster mode was used to scribe on samples and generate LIG. Various parameters can be modified in the laser. The speed of the moving lens system (S) can be chosen from 1% to 100% of the maximum in 1% increments. The same is applied to beam power (P), with a maximum value of 30 W. 1200 DPI resolution and autofocus mode were selected. Besides, the laser has two utilities. Air Assist blows compressed air on the lased material surface, removing heat and combustible gases,[89] while the gas extractor (BOFA AD Base2) takes away expelled gases.

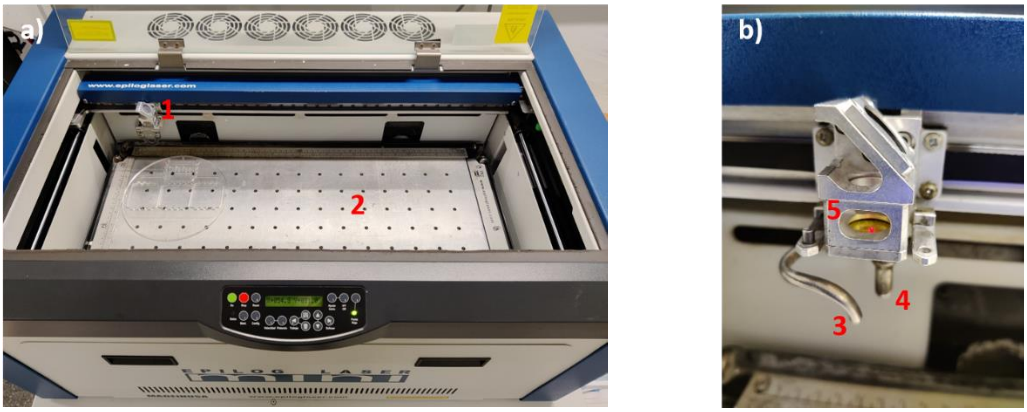

Figure 10. *a) Epilog Legend Mini 24 (1: Lens moving head. 2: Sample stage.). b) Lens moving head (3: Air Assist expeller. 4: Autofocus sensor. 5: Focusing lens).*

Before every use, the focusing lens was cleaned with a cotton swab moistened in Epilog Laser Multi-Coated Filter and Lens Cleaner liquid to minimize power lowering by contamination.[89] A preliminary study of the system was performed (ANNEX I), concluding that incident power differs depending on stage position. It was seen that laser power decreases in locations away from the source, especially in the Y axis with the extractor switched on. Therefore, experiments were performed close to the beam source, with the extraction system switched off. A flat glass panel was employed as substrate holding base. To end the system pre-analysis, the actual resolution and lased spot size were studied and compared with the manual value (ANNEX II).

It is important to emphasize the difficulty to find the parameters to obtain LIG in each material. A few percentile units on S and P make the difference between obtaining LIG and not modifying or perforating the material. Moreover, only products that contain LIG can be characterized electrically to refine parameters. Consequently, at first, S, P, lasing steps and focusing distance were varied on studied samples. Trial and error would imply a too large score of experiments, so the procedure described next was performed.

CONDITION MATRIX METHOD

Using CorelDRAW X7 software, 7x7 matrixes of 4x4 mm^2 squares were designed with a S and P value for each column and line, respectively (Figure 11). After lasing, obtained LIG was electrically characterized when possible, but a visual inspection was enough to identify lack of LIG. The range and increasing step of the matrixes were adapted iteratively to get closer to LIG yielding conditions. This process was done in cardboard with three types of coating: i) FRS, ii) FG, and iii) lignin with NC.

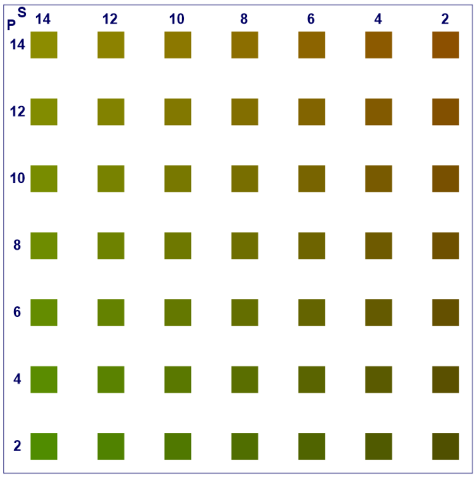

Figure 11. *a) Matrix designed in CorelDRAW with P (lines) and S (columns) ranging from 2 to 14, with 2 unit steps.*

In cardboard samples treated with fire retardants no LIG was obtained with a single lasing, so multiple lasing steps were done to study its influence. Defocusing 1 mm, 1.5 mm, and 3 mm was also tried. The search was finalized engraving the matrixes shown in Figure 15. LIG obtained in each condition will be labelled with the following system: *Pretreatment_LIG_SXPY_Xmm* (to indicate coating material, speed, power, and defocus that was used).

3.3. LIG CHARACTERIZATION METHODS

ELECTRICAL CHARACTERIZATION

The R_s was used as comparative figure to choose the least resistive samples for further electrochemical and morphological characterization. Van der Pauw method[69] measurements were performed on the square LIG samples with a four-point probe station (EP6, Suss MicroTec) and a Keysight B1500A Semiconductor Device Analyzer. Current values from 0 to 2 mA with 4 µA steps were employed. The current was forced parallel to the raster direction and perpendicular to it, obtaining two R_s values, $R_{s,parallel}$ and $R_{s,perpendicular}$. This aimed to analyse the resistivity anisotropy of LIG. The repeatability of LIG was studied preparing N=4 squares (4x4 mm^2) in the 6 best conditions on organic substrates and in PI, and measuring their two R_s values.

ELECTROCHEMICAL CHARACTERIZATION

First, a preliminary study was carried out to test whether LIG obtained in the condition that yield lowest R_s in every organic substrate could be used as a working electrode. WE electrodes of LIG (N=4) were prepared with the design of Figure 12a. A preactivated-carbon screen-printed electrode (SPE) was also employed, as a WE gold-standard control. An electrochemical cell was assembled with each WE, a commercial Ag/AgCl RE and a Pt CE, all submerged in PBS with 100 mM ferricyanide and 1 M KCl (702587 and P3911 from Sigma-Aldrich). Using a Palmsens4 potentiostat, CVs at 20 $mV \cdot s^{-1}$ were performed. Voltage window was set from -0.6 V to 0.8 V for FRS_LIG and SPE, and from -0.8 V to 1.0 V for FG_LIG. Coating of LIGNIN+NC_LIG has had problems of mechanical instability in DI water, so only a CV experiment at different scan rates was performed, and it was discarded for further electrochemical studies (ANNEX III).

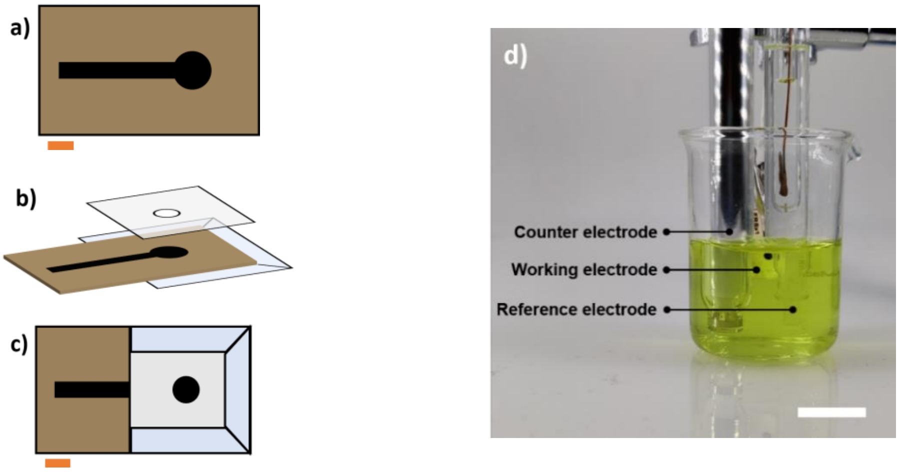

Figure 12. *a) Corel design of WE (scalebar, 2 mm). b) Manufacturing of WE. c) Manufactured WE (scalebar, 2 mm) (elaborated by the author). d) Electrochemical cell setup for CV experiments with CE in the left, RE in the right and WE at the back, submerged in 30 ml solution (scalebar, 2 cm).*

Electrodes' surface area and electron transfer of LIG electrodes from PI and coated cardboard substrates were studied by CVs at 5, 10, 20, 50, 75 and 100 $mV \cdot s^{-1}$ in 10 mM ferricyanide (N=4).

MORPHOLOGICAL CHARACTERIZATION

The LIG samples created for repeatability analysis were further studied using a Scanning Electron Microscope (SEM, Carl Zeiss Auriga model). 1 kV electron acceleration was used for sample surface and cross-section imaging. In order to take cross-section pictures, the samples were cut with a scalpel. A stage with metal tweezers was employed to contact samples that showed drift issues at high magnification analysis (15Kx).

3.4. DEVICE DESIGN, FABRICATION AND CHARACTERIZATION

SUPERCAPACITORS

The design described in Figure 13a was scribed on PI and FRS treated cardboard to obtain interdigitated LIG electrodes, with S9P9[45] and S9P11_3mm parameters, respectively. As explained in ANNEX IV, each substrate needed a different CorelDRAW design. The resistance of the scribed LIG design was measured with a multimeter (Fluke 73-III).

A supercapacitor electrolyte was prepared using 10% w/v PVA / 1M H_2SO_4, a gold-standard in literature.[29,31,42,49] 0.5 g PVA (343126 from Sigma-Aldrich) were dissolved in DI water at 90 °C. When cooling to 60 °C, 0.27 ml 96% H_2SO_4 (131058 from PanReac AppliChem) were added and mixed at 90 °C to obtain the electrolyte. After storing the electrolyte overnight at 4 °C it was used at room temperature to build supercapacitors.

The LIG electrodes were employed to yield prototype SCs according to design illustrated in Figure 13b (3 of each substrate). SCs were manually assembled and characterized. First, the resistance was measured with a multimeter. Then, CV experiments at 10, 50 and 100 $mV \cdot s^{-1}$ were performed in a potential window from 0 V to 0.8 V, employing Palmsens4 potentiostat. Finally, galvanostatic charge discharge curves were measured up to 0.4 V or 0.8 V maximum voltage. For PI_LIG SCs 1 µA and 5 µA were used, and 20 µA and 50 µA for FRS_LIG SCs. It must be stated that between each CV and GCD experiment SCs were discharged short-circuiting the electrodes with a metallic wire.

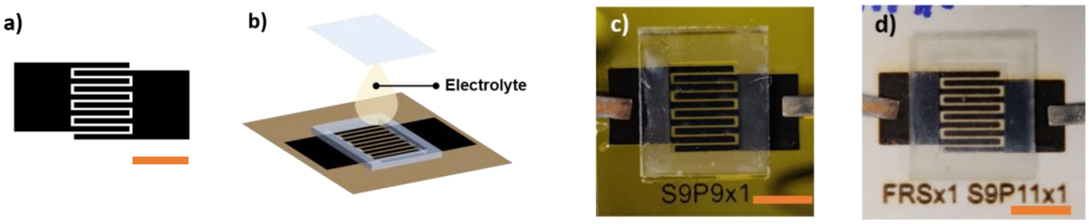

Figure 13. *a) Corel design of interdigital electrodes . b) Illustration of SC manufacturing process. c) PI_LIG_SC under measurement. d) FRS_LIG_SC under measurement. (Scalebars, 5 mm).*

BATTERIES

First, a bio-polymeric ion exchange membrane was synthetized based on a protocol developed by the SPEED group. This is composed of 2 w/v % alginate (W201502 from Sigma-Aldrich) and 1 w/v % NC at 75:25 ratio, with an additional 5 w/v % glycerol (G9012 from Sigma-Aldrich). For the alginate dispersion, 1 g alginate was stirred in 50 ml DI water at 80 °C until completely dissolved. The NC dispersion was prepared as explained for the lignin pretreatments. Both were mixed in 75:25 ratio and 2.4 ml glycerol were later added to the 60 ml dispersion. After mixing overnight, 15 ml of the obtained hydrogel was poured in a Petri dish. Water evaporation by incubation at 25 °C overnight yielded the desired membrane.

Second, biobased matrix electrodes were prepared, again based on a protocol by the SPEED group. For the cathode, the constituent matrix was made of 25:75 alginate and NC, with 5 w/v % glycerol, prepared as explained for the membrane. This was doped with 0.25 M oxalic acid and 0.2 M iron (III) nitrate (O0376 and 254223 from Sigma-Aldrich). The anodic constituent matrix is composed of 75:25 alginate and NC, with 5 w/v % glycerol. It was doped with 0.1 M KOH and 0.1 M L-ascorbic acid (60370 and A0273 from Sigma-Aldrich).

The electrode design described in Figure 14a was produced with PI_LIG_S9P9 and FRS_LIG_S9P11_3mm. 260 µl of anodic matrix were dispensed in 3 LIG current collectors of each type, and the same with the cathodic matrix to form 3 other electrodes of PI_LIG and FRS_LIG. These electrodes were dried overnight at 25 °C in an incubator.

Once the constituents of the batteries were fabricated, these were joined as shown in Figure 14b to build 4 batteries, two of each substrate. First, the battery open circuit voltage was measured. Then, a linear sweep voltammetry was performed from the OCV value to short-circuit, with 20 mV·s^{-1} scan rate. The LSV was carried out both pressing the electrodes and without applying pressure, letting the OCV recover before each measurement.

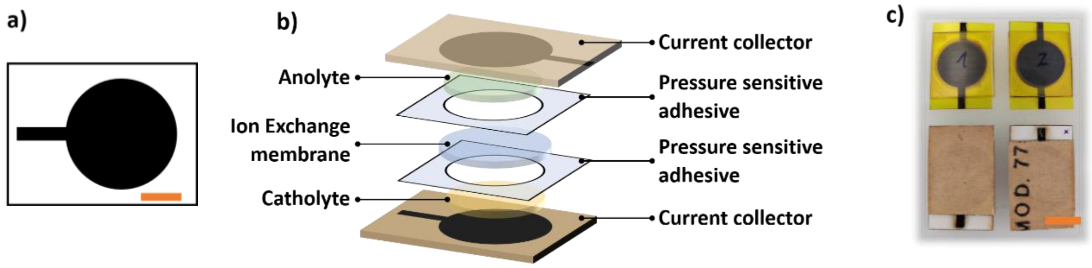

Figure 14. *a) Corel design of battery current collectors (scalebar, 5 mm). b) Illustration of battery manufacturing process. c) PI_LIG_Batteries (top) and FRS_LIG_batteries (bottom) (scalebar, 1 cm).*

4. RESULTS AND DISCUSSION

4.1. OPTIMIZED LASING CONDITIONS

Based on their lower sheet resistance, the following lasing conditions resulted to be the best for each treatment of cardboard samples: i) S9P11_3mm and S10P11_3mm for FRS spray, ii) S8P11_3mm and S9P11_3mm for FG spray, and iii) S8P11 and S10P12 for NC+LIGNIN coated cardboard. For this latter one, evaporation of hydrogel in a Petri dish has resulted the most homogeneous lignin enhancing treatment (ANNEX V).

The LIG samples produced in the matrixes shown in Figure 15 gave the lowest R_s values for every treatment (Figure 16). A direct observation is that LIG is anisotropic in terms of conductivity, i.e. for the same lasing conditions $R_{s,parallel}$ is one order of magnitude smaller compared to $R_{s,perpendicular}$. This may be caused by LIG's anisotropic fabrication, as the lowest R_s is measured in the direction that the laser follows when rastering the sample (along X axis). This observation has not been previously reported in literature.

Furthermore, LIG's conductivity does not follow a smooth tendency when varying P and S, but rather a slightly randomised parabola. This may be due to the critical effect of correlation of P and S to give best reaction conditions for LIG formation. Every square is produced in a different XY position of the stage, and the varying incident power may have also affected (ANNEX I). However, some small tendencies can be observed to choose best fabrication conditions. Both $R_{s,parallel}$ and $R_{s,perpendicular}$ are lowest at P11 for the three substrate pretreatments. As for S, higher values are needed to obtain LIG in FRS than in FG, so it seems FG protects more the substrate from burning. However, measured R_s is lowest near S8-S10 for both FRS and FG. Therefore, S8P11_3mm and S9P11_3mm are chosen as best conditions for FG_LIG, and S9P11_3mm and S10P11_3mm for FRS_LIG. In contrast, LIGNIN+NC_LIG presents low R_s in a wider range of S and P, especially in S7-11 and P10-12 ranges. For these reasons, S8P11 and S10P12 have been chosen as most suitable conditions. At this point, it is important to highlight that all conditions optimized to produce LIG consist of just one lasing step. This is very interesting for time and energy optimization, especially in case the process is scaled to industry level.

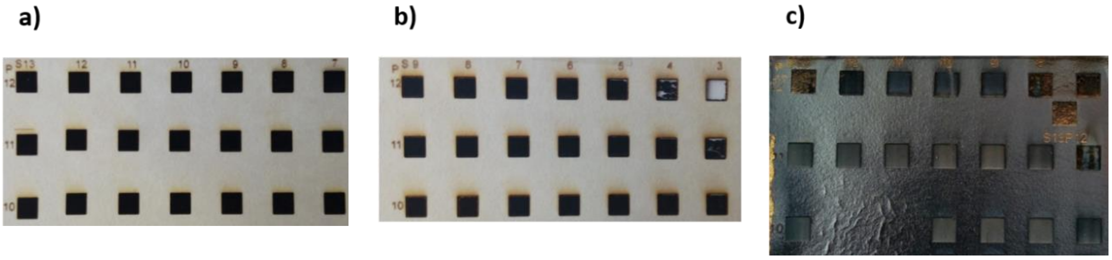

Figure 15. *Final matrixes (4x4 mm² squares as scalebar) for different cardboard treatments. a) FRS sprayed cardboard (S7-13P10-12 and 3mm defocus). b) FG sprayed cardboard (S3-9P10-12 and 3mm defocus). c) LIGNIN+NC coated cardboard (S7-13P10-12, focused).*

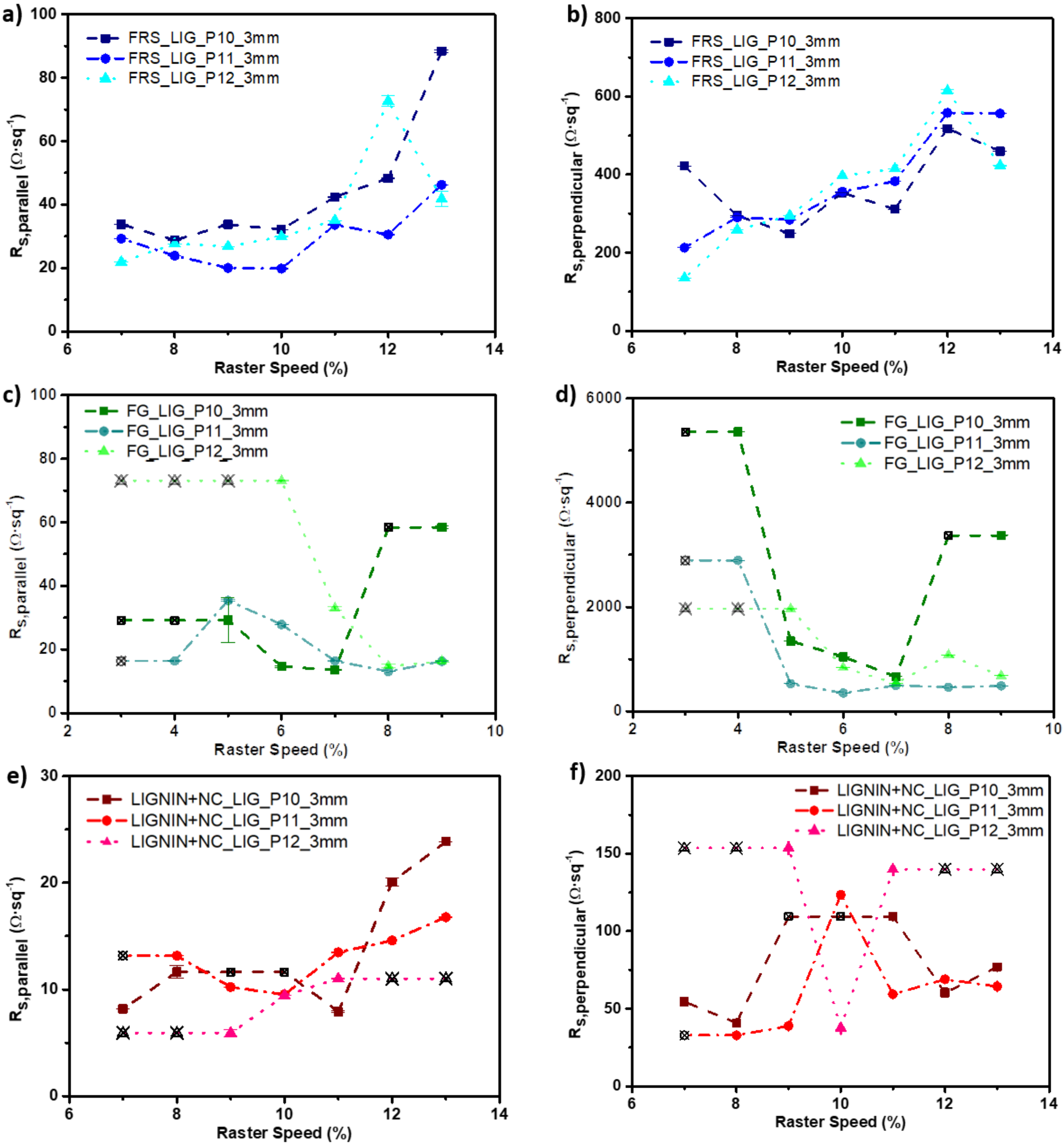

Figure 16. *Rs,parallel measurements of LIG in different conditions and treatments: a) FRS_LIG with 3 mm defocus c) FG_LIG with 3 mm defocus e) LIGNIN+NC_LIG focused. Rs,perpendicular measurements of LIG in different conditions and treatments: b) FRS_LIG with 3 mm defocus d) FG_LIG with 3 mm defocus f) LIGNIN+NC_LIG focused.*

Regarding the repeatability of LIG, the 3 most similar replicas of each condition have been chosen, discarding outliers (Figure 17). PI_LIG_S9P9 shows most repeatable R_s, with 29.5 ± 0.4 $\Omega\cdot sq^{-1}$ for $R_{s,parallel}$, in the same order of magnitude as in the literature[31]. LIGNIN+NC_LIG_S8P11 presents lowest R_s values, with a very repeatable figure of 8.1 ± 0.4 $\Omega\cdot sq^{-1}$. This competes with the lowest R_s in the literature for biobased substrate derived LIG, 3.8 $\Omega\cdot sq^{-1}$, which was obtained with high boric acid contents.[43] Moreover, it easily outranks other LIG types reported in the literature, so not only has a new LIG technique been developed, but it is highly promising for future studies. The principal cause is probably that a higher lignin content causes less defects on obtained graphene, because aliphatic carbon parts are more easily decomposed compared with aromatic carbon.[40] As for LIG obtained in fire retardant treated cardboard, it has higher standard deviation. Moreover, R_s values are around 30-40 $\Omega\cdot sq^{-1}$, larger than those obtained in matrixes, even though the order of magnitude is maintained. FRS_LIG_S9P11 presents lowest $R_{s,perpendicular}$ (149±25 $\Omega\cdot sq^{-1}$) and FG_LIG_S9P11 lowest $R_{s,parallel}$ (29.1±2.6 $\Omega\cdot sq^{-1}$), in terms of fire-retardant treated cardboard samples. LIGNIN+NC_LIG_S10P12 could not be reproduced, maybe due to a different composition or inhomogeneity of the lignin and NC coating of the cardboard.

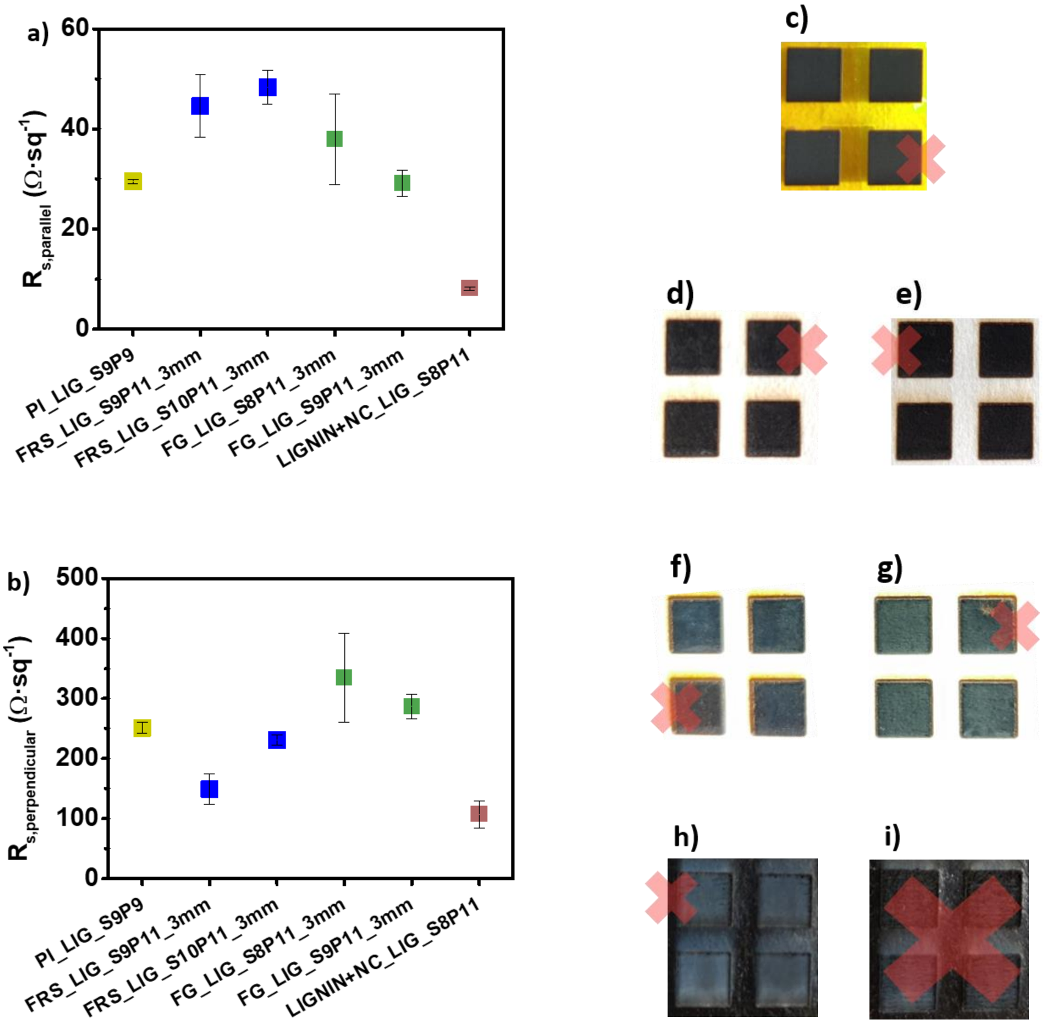

***Figure 17.** a) Rs,parallel of LIG in different substrates, treatments, and conditions. b) Rs,perpendicular of LIG in different substrates, treatments, and conditions. N=4 4x4 mm^2 squares in each substrate, treatment and condition with discarded samples crossed out: c) PI_LIG_S9P9 d) FRS_LIG_S9P11_3mm e) FRS_LIG_S10P11_3mm f) FG_LIG_S8P11_3mm g) FG_LIG_S9P11_3mm h) LIGNIN+NC_LIG_S8P11 i) LIGNIN+NC_LIG_S10P12.*

4.2. LIG AS ELECTRODIC SURFACE

Cyclic voltammograms of 100 mM ferricyanide (ANNEX VI) demonstrate that LIG derived from cardboard can be used as WE in an electrochemical cell. To the best of our knowledge, this is the first experiment reported in literature that demonstrates LIG capability for electron transfer in a redox reaction. It has also been tested that FRS_LIG_S9P11 and FG_LIG_S8P11 have better performance as electrode surfaces, compared to the other conditions selected for FRS- and FG-treated cardboard. They have higher peak currents and smaller oxidation- and reduction-peak voltage difference.

CV experiments of 10 mM ferricyanide performed at increasing scan rates result in the diagrams shown in Figure 18. The ECSAs of SPE and PI_LIG electrodes have been calculated with eq. (2), as they represent electrochemically reversible systems. Eq. (3) has been used for FRS_LIG and FG_LIG electrode containing systems, which are quasi-reversible. This is deduced from reduction and oxidation peak intensity ratio (approx. 1 for the former and around 0.8 for the latter). ECSA has been compared with the geometrical area (GA). The resulting ratio is shown in Table 1. In conclusion, FRS_LIG and FG_LIG have a 3D surface structure (ECSA/GA ~ 2), while SPE has a 2D surface and PI_LIG's surface is shows a combined behaviour of 2D and 3D structure. The standard heterogeneous electron transfer rate constant (k^o, cm·s^{-1}) has also been calculated based on peak-to-peak voltage difference. Eq. (4) has been used for PI_LIG and SPE, whereas eq. (6) has been employed at 5 mV·s^{-1} scan rate CVs for FRS_LIG and FG_LIG (increasing scan rate decreases k^o, as expected from the voltammogram charge transfer slope change).

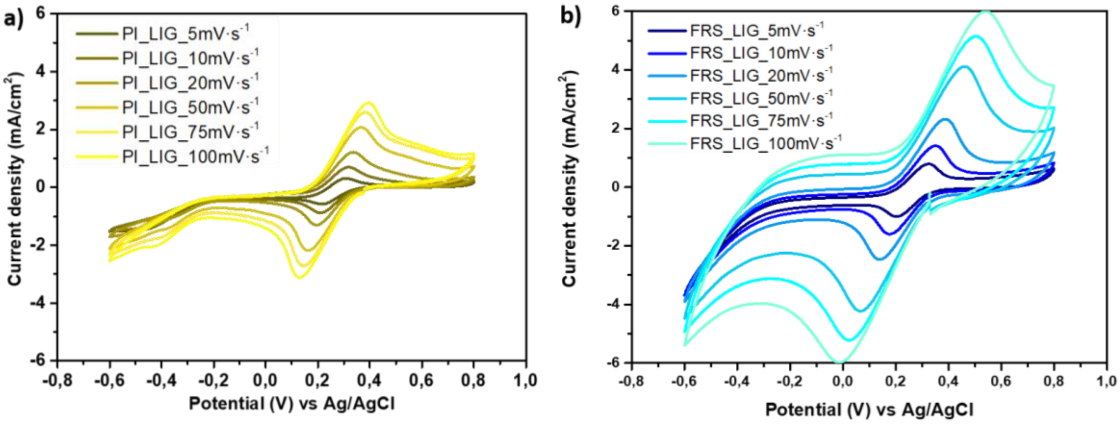

Figure 18. *CVs at different scan rates. a) In PI_LIG_S9P9 electrodes. b) In FRS_LIG_S9P11_3mm electrodes.*

Table 1. ECSA/GA ratios and k° for different electrode types.

ELECTRODE	SPE	PI_LIG _S9P9	FRS_LIG_S9P11_3mm	FG_LIG_S8P11_3mm
ECSA/GA	0.897 ± 0.024	1.29 ± 0.08	2.11 ± 0.06	2.2 ± 0.7
k^o (cm·s^{-1})	0.00188 ± 0.00010	0.0023±0.0003	0.00046 ± 0.00008	0.00016 ± 0.00007

The result cannot be compared with figures from the literature as no electrochemical characterization of laser-induced graphene has been reported so far. Therefore, this study could serve as a means for comparison in future research on this aspect.

SEM pictures in low magnification demonstrate again anisotropy of LIG, in the form of blurry lines in the direction of laser rastering, which may cause the difference in $R_{s,parallel}$ and $R_{s,perpendicular}$ (Figure 19a,c). This appearance has recently been reported and confirmed with analysis of diffuse scattering of light in LIG surface.[90] However, resistivity anisotropy has not been reported before, so this is the first time it is related with morphological anisotropy.

In high magnification images, LIG morphology is very different depending on the pretreatment of cardboard. FRS_LIG and FG_LIG present a hierarchical highly porous structure (Figure 19a,b), with different pore sizes ranging from macropores (larger than 50 nm diameter) to mesopores (2-50 nm diameter). This has been reported for other LIG types.[31,40,49] PI_LIG does not present pores, but a very rough surface (Figure 19e). The two morphological natures can be directly related to ECSA/GA ratios from Table 1.

As for LIGNIN+NC_LIG, in high magnification SEM images it presents long filaments with a width ranging from tens to hundreds of nanometres (Figure 19c,d). These carbonaceous elongated nanostructures may be responsible for such low R_s values of LIGNIN+NC_LIG. The formation of carbon nanotubes (CNT) in the production of LIG by multiple lases on PI has already been reported.[53] Moreover, laser vaporization has been proven as an established method for the production of CNTs.[91] However, this is the first time carbonaceous nanowires are produced with LIG by a single lase, and from a biobased organic precursor.

Finally, thickness of produced LIG with different pretreatments and lasing conditions can be estimated from the cross-section images (Figure 19f). These figures are gathered in Table 2. Even though the mechanical cut with the scalpel may have distorted the morphology and thickness of LIG, some conclusion can be extracted. As expected, porous LIG thickness (cardboard derived) is larger compared with non-porous LIG (obtained from PI), with around 170 µm and 38 µm thickness, respectively, because material expands like a foam.[43] This indicates that LIGNIN+NC_LIG is probably porous as well. It could also be deduced from the cross-section image of the sample, where LIG expands upwards from the coating surface. This porosity of cardboard derived LIG has great importance for application in electrochemical conversion or storage systems. It is a great benefit to have a larger electrochemically active surface area, as performance parameters such as power or intensity of devices are directly related to the ECSA.

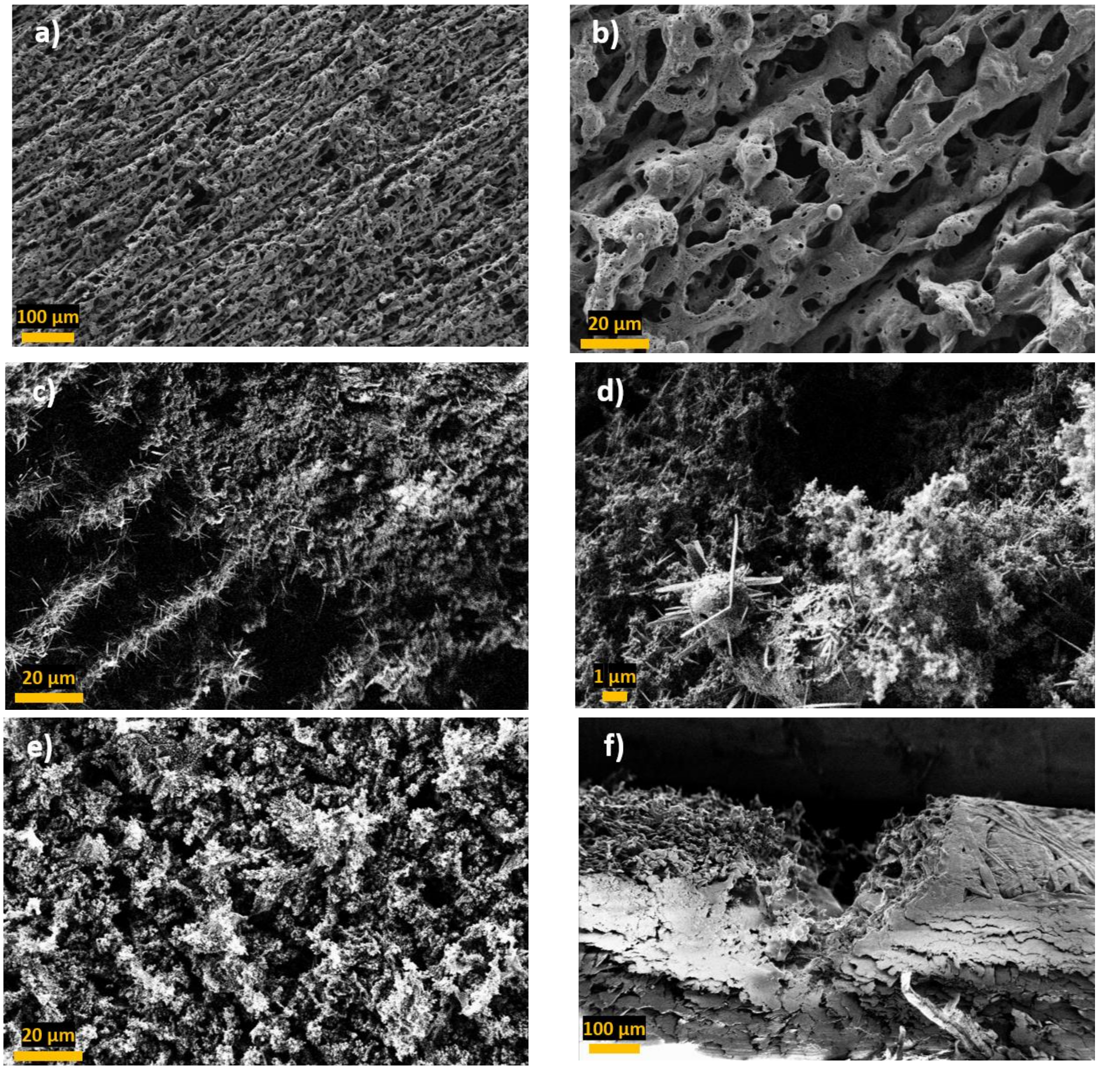

Figure 19. *SEM images of sample surfaces: a) and b) FG_LIG_S9P11_3mm. c) LIGNIN+NC_LIG_S10P12. d) LIGNIN+NC_LIG_S8P11. e) PI_LIG_S9P9. Cross section: f) FG_LIG_S8P11_3mm.*

Table 2. Thickness of produced LIG in different substrates.

Condition	Thickness (µm)
PI_LIG_S9P9	37.5 ± 1.0
LIGNIN+NC_LIG_SP11	171.2 ± 2.5
FRS_LIG_S10P11_3mm	182 ± 11
FG_LIG_S8P11_3mm	164 ± 9

4.3. LIG APPLICATION FOR ENERGY STORAGE

SUPERCAPACITORS

Concerning resistance measurements of scribed interdigitated electrodes, they present values out of range of the multimeter (20 MΩ), both with PI and cardboard based LIG. This means they are not short-circuited and can be used to build SCs. As explained in ANNEX VII, it has not been possible to build interdigitated electrodes with FG_LIG. Thus, FRS treated cardboard and PI derived devices (with FRS_LIG_S9P11_3mm and PI_LIG_S9P9 conditions) will be discussed.

The CVs performed by each SC are illustrated in Figure 20. Cardboard based SCs present higher currents and cyclic voltammogram areas. Thus, their C_A is greater than PI based SCs at all scan rates (e.g. 1.60 mF·cm^{-2} and 0.19 mF·cm^{-2} at 10 mV·s^{-1}, respectively), as observed in Table 3. It can be concluded that, cardboard SCs store more charge when applying the same voltage. This agrees with its morphological structure, as it presents higher ECSA/GA ratio (2, instead of 1 in PI_LIG), providing more available sites where ions from electrolyte can be adsorbed. However, cardboard derived SCs have less rectangular shaped cyclic voltammograms. The steeper slope indicates a major current leakage between electrodes, caused by a lower parasitic resistance. This makes self-discharge of cardboard SCs faster. The reason for this may be that acid polymer electrolyte damages cardboard substrate, compromising LIG integrity and causing electrodes to be less isolated from one another.

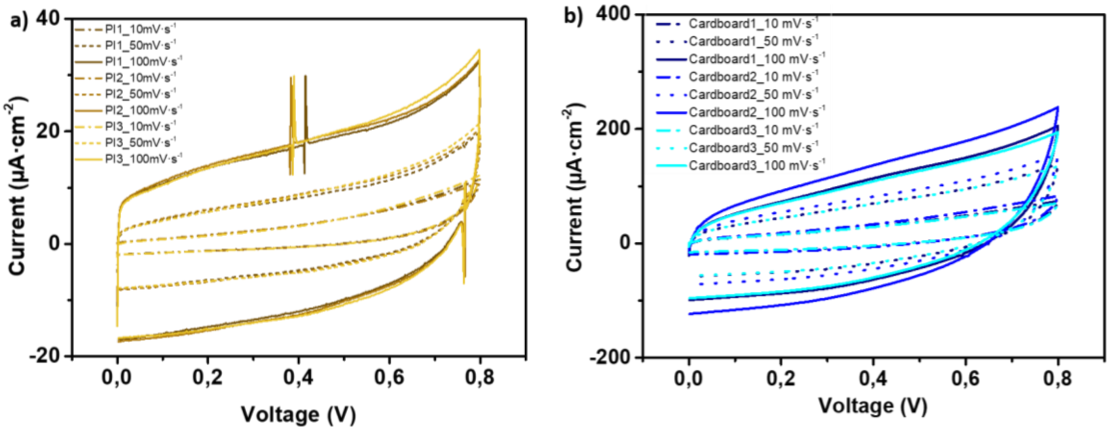

Figure 20. *CVs at different scan rates. a) For SCs based on PI. b) For SCs based on cardboard.*

Table 3. Areal capacitance (in mF·cm^{-2}) calculated from CVs with equation (6).

Scan rate (mV·s^{-1})	PI based SCs	Cardboard based SCs
10	0.1863 ± 0.0021	1.60 ± 0.18
50	0.126 ± 0.004	0.98 ± 0.12
100	0.142 ± 0.003	0.81 ± 0.11

Some representative galvanostatic charge-discharge curves performed in each SC are shown in Figure 21, while in Table 4 figures calculated from these results are gathered. GCD curves of PI based SCs are closer to an ideal triangular shape than those built on cardboard. This is reflected also in their smaller relative difference of C_A calculated from eq. (7) and (10) (0.191 and 0.164 mF·cm^{-2}). However, they are not completely ideal, as shown in the C_A calculated by both methods, considering the area and the slope of the discharge curve. Even though, they present higher coulombic and energy efficiencies (ca. 70% and 50%), with imperceptible voltage drop in discharge. As for cardboard SCs, they yield higher effective areal capacitance (0.75 mF·cm^{-2}), as in CVs. The major cause for lower efficiencies in cardboard SCs is the large voltage drop in discharge. From this voltage loss an equivalent series resistance of 1.8 ± 0.3 kΩ can be estimated.

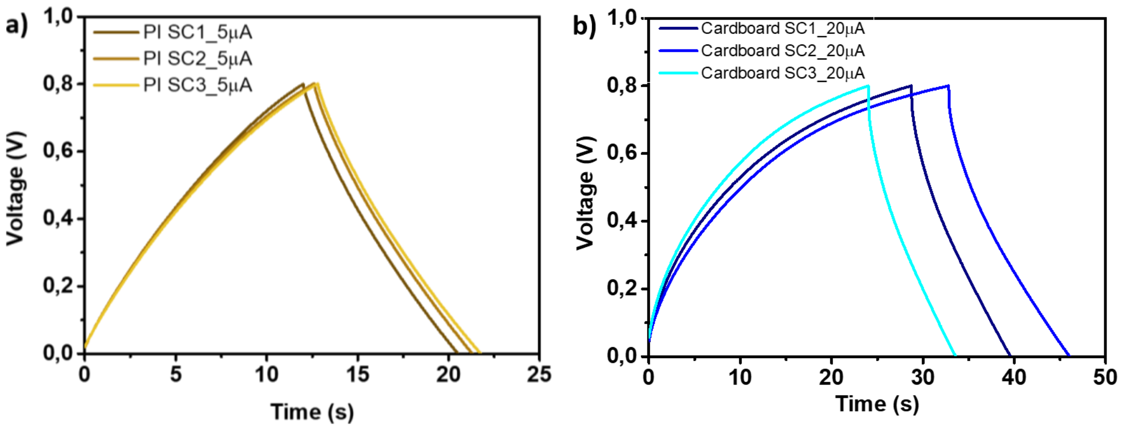

Figure 21. *a) GCDs for SCs based on PI at 5 µA. b) GCDs for SCs based on cardboard at 20 µA.*

Table 4. Figures calculated from GCD experiments.

Figure	**PI_LIG_S9P9 SCs (5 µA, 0-0.8 V)**	**FRS_LIG_S9P11_3mm SCs (20 µA, 0-0.8 V)**
CA from equation (7) (mF·cm^{-2})	0.191 ± 0.006	1.08 ± 0.17
CE (%)	70.1 ± 0.9	39.0 ± 1.4
EE (%)	50.4 ± 1.1	21.1 ± 0.6
CA from equation (10) (mF·cm^{-2})	0.164 ± 0.004	0.75 ± 0.13

In general, PI based SCs have shown better efficiencies, more ideal behaviour, and higher reproducibility. This was predictable, as PI_LIG_S9P9 has already shown lower and more reproducible R_s values. However, cardboard derived SCs have better areal capacitance. This agrees with the fact that LIG produced with FRS treatment in cardboard presents 3D surface in CV experiments and a highly porous morphology in SEM images.

PI based SCs reported in this work present C_A of around 0.2 mF·cm^{-2}, lower than 1-4 mF·cm^{-2} published by J. Lin et al.[31] It must be stated that geometries are different. Taking into account the whole area of the capacitor instead of just the interdigitated electrodes, the C_A of PI based SCs from this work and from the literature would get more similar. However, cardboard derived SCs do present C_A values of the same order of magnitude as those reported in the literature for LIG (around 1 mF·cm^{-2}).[92]

BATTERIES

The general figures of PI_LIG and FRS_LIG based batteries are gathered in Table 5. They both present similar OCV values (approx. 1 V), which are very stable (Figure 22a). As for the output intensity and maximum power of both batteries, it depends on whether pressure is applied to the device or not (Figure 22b,c). The different battery layers were glued together with pressure sensitive adhesive. When pressing the battery, the different layers are better compacted improving the whole battery structure. The contact between the electrodes and membrane is enhanced, and thus the battery presents better performance, i.e. higher current and power.

In comparison, the output maximum power provided by PI based batteries is much higher than that of cardboard batteries (0.4 mW at 0.9 mA and 30 µW at 66 µA, respectively, in Figure 22b,c). This is linked to the lower intrinsic resistance of PI_LIG current collectors. Furthermore, when drop casting anodic and cathodic matrix hydrogels on cardboard LIG current collectors, some of it was absorbed by the cardboard. Therefore, available species concentration is lower on cardboard batteries, contributing to the reduction of the maximum power output. As seen for SCs, batteries made of PI derived LIG present higher repeatability than those of cardboard. This is attributed to the better repeatability of LIG on PI, as explained in its electrical and electrochemical characterization. Finally, as can be seen in LSV curves, these batteries have fundamentally ohmic losses, particularly those built with LIG produced on cardboard.

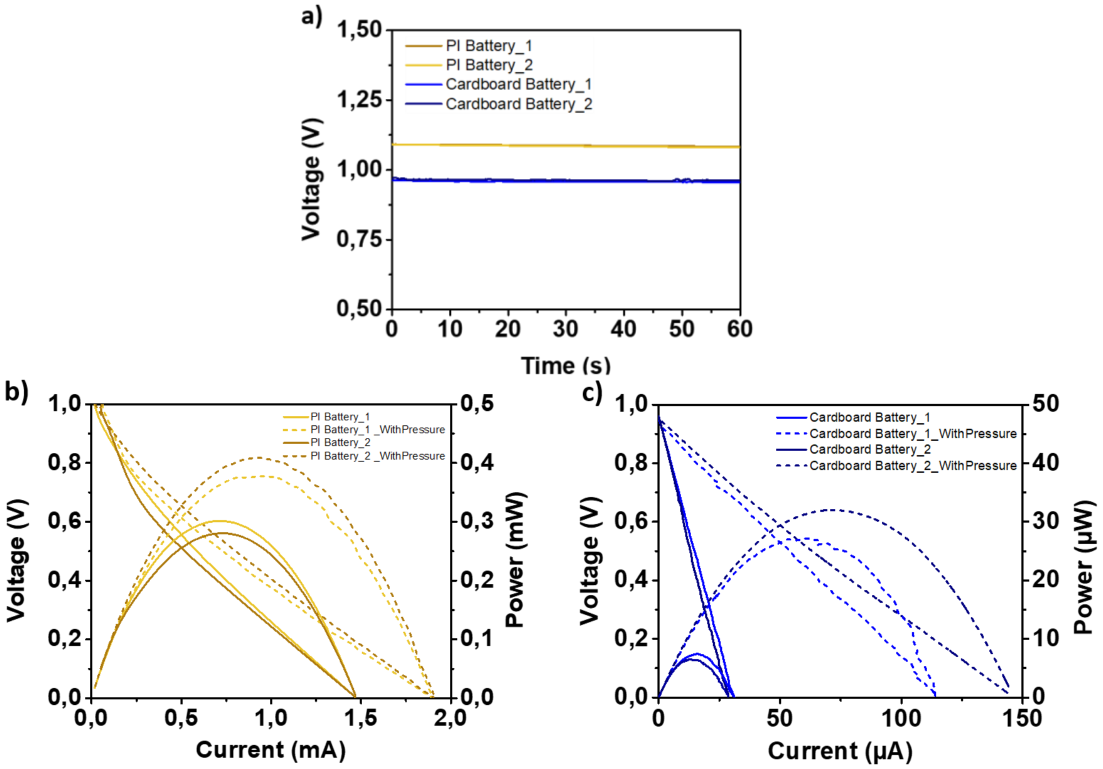

Figure 22. *a) OCVs for manufactured batteries, with pressure applied. b) LSV and power output characteristic for battery based on Kapton and power output. c) LSV and power output characteristic for battery based on cardboard.*

Table 5. Figures calculated for PI and cardboard based batteries.

Figure	PI batteries	Cardboard batteries
OCV	1.0867 ± 0.0016 V	0.961 ± 0.004 V
Max. power	0.393 ± 0.022 mW	30 ± 3 µW
Current density for max. power	0.937 ± 0.008 mA	66 ± 6 µA

This is the first time bare LIG is used to make battery devices. Therefore, no previous reference has been found to compare the performance accomplished in this project. Moreover, it is the first proof of concept of a biopolymer-based cardboard battery that has been developed. Consequently, this work opens a new path in the research of fully recyclable, biodegradable or even compostable batteries.

5. CONCLUSION

Laser-induced graphene has been obtained from organic bio-based precursors, and the laser conditions for its fabrication have been optimized. The produced LIG has been electrically, electrochemically, and morphologically characterized. As for resistivity, anisotropic behaviour has been found in LIG derived from all substrates. The best performance has been obtained in cardboard coated with the newly developed lignin and nanocellulose surface treatment, with an 8.1 $\Omega \cdot sq^{-1}$ sheet resistance value. Electrochemical characterization has demonstrated that cardboard derived LIG has 3D electroactive surface structure, which is beneficial for electrochemical energy storage application. However, a lower transfer coefficient has been obtained compared with its polyimide derived plastic competitor. Scanning electron microscope images have shown that surface morphology is highly porous and anisotropic for cardboard derived LIG, which agrees with electrical and electrochemical properties.

To reach the main goal of this work, optimized cardboard derived LIG has been employed in the development of electrochemical energy storage devices. On the one hand, supercapacitors manufactured with cardboard-LIG have shown higher areal capacitance in comparison to polyimide based SCs. Moreover, achieved 1 $mF \cdot cm^{-2}$ areal capacitance is of the same order of magnitude as values found in the literature. Nevertheless, cardboard based SCs present high leakage current and series resistance. On the other hand, it has been possible to use bare LIG as current collector on biopolymer-based batteries, with both cardboard and PI as substrate. Even though PI derived batteries have demonstrated better performance, cardboard batteries have proved to deliver a maximum power of 30 µW. Thus, they could already have some applications to power low-consumption sensing and monitoring devices as a disposable energy source.

Although initial objectives have been completed, many interesting paths have arisen in the development of this project. First, it must be remembered that the developed lignin and nanocellulose coating has demonstrated to be a very promising treatment to obtain high performance LIG on cardboard. Therefore, further studies should be carried out to enhance its properties to lead its implementation in many applications.

As for the developed batteries and supercapacitors, despite the initial substrate is bio-based and recyclable, a standardized thorough analysis should be performed to ensure that the final product is non-toxic and does not compromise current cardboard and paper recycling methods. Depending on the obtained results, new materials could be chosen for future optimization and application diversification. As shown on Figure 23, this project stands as the first loop in a cyclic improvement for the development of sustainable energy storage devices using LIG electrodes. In every loop, literature research helps selecting materials to study and optimize laser conditions for LIG production. After its characterization, it is implemented in devices, which should be analysed in terms of sustainability, later to continue the cycle.

In conclusion, this project has taught me that the path to sustainable technology development is not straightforward, but highly demanding and rigorous. However, the price of changing the actual energy storage paradigm into more environmentally friendly models deserves the effort. This work is just a tiny part of this transition, but I believe every little act helps in the exciting and challenging research towards more sustainable and responsible technology.

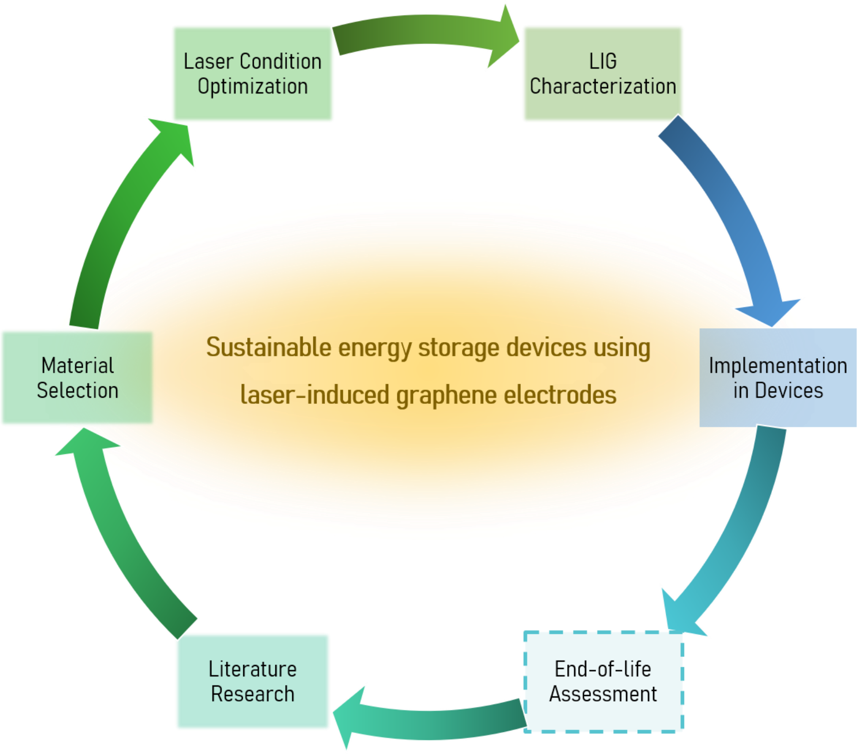

Figure 23. *Schematic concept illustration showing the cyclic process for the development of sustainable energy storage devices using LIG electrodes.*

6. REFERENCES

(1) Anderegg, W. R. L.; Prall, J. W.; Harold, J.; Schneider, S. H. Expert Credibility in Climate Change. *Proc. Natl. Acad. Sci. U. S. A.* **2010**, *107* (27), 12107–12109. https://doi.org/10.1073/pnas.1003187107.

(2) Arrhenius, P. S. XXXI. On the Influence of Carbonic Acid in the Air upon the Temperature of the Ground. *London, Edinburgh, Dublin Philos. Mag. J. Sci.* **1896**, *41* (251), 237–276. https://doi.org/10.1080/14786449608620846.

(3) UNFCCC. *Adoption of the Paris Agreement Report No. FCCC/CP/2015/L.9/Rev.1*; Paris, 2015.

(4) Fawzy, S.; Ahmed, ·; Osman, I.; Doran, J.; David, ·; Rooney, W. Strategies for Mitigation of Climate Change: A Review. **2020**, *18*, 2069–2094. https://doi.org/10.1007/s10311-020-01059-w.

(5) Gielen, D.; Boshell, F.; Saygin, D.; Bazilian, M. D.; Wagner, N.; Gorini, R. The Role of Renewable Energy in the Global Energy Transformation. *Energy Strateg. Rev.* **2019**, *24*, 38–50. https://doi.org/10.1016/j.esr.2019.01.006.

(6) Hoffert, M. I.; Caldeira, K.; Benford, G.; Criswell, D. R.; Green, C.; Herzog, H.; Jain, A. K.; Kheshgi, H. S.; Lackner, K. S.; Lewis, J. S.; Lightfoot, H. D.; Manheimer, W.; Mankins, J. C.; Mauel, M. E.; Perkins, L. J.; Schlesinger, M. E.; Volk, T.; Wigley, T. M. L. *Advanced Technology Paths to Global Climate Stability: Energy for a Greenhouse Planet*.

(7) Ibrahim, H.; Ilinca, A.; Perron, J. Energy Storage Systems-Characteristics and Comparisons. *Renewable and Sustainable Energy Reviews*. Pergamon June 1, 2008, pp 1221–1250. https://doi.org/10.1016/j.rser.2007.01.023.

(8) Luo, X.; Wang, J.; Dooner, M.; Clarke, J. Overview of Current Development in Electrical Energy Storage Technologies and the Application Potential in Power System Operation. *Appl. Energy* **2015**, *137*, 511–536. https://doi.org/10.1016/j.apenergy.2014.09.081.

(9) European Commission, D.-G. for E. *Powering a Climate-Neutral Economy: An EU Strategy for Energy System Integration. COMMUNICATION FROM THE COMMISSION TO THE EUROPEAN PARLIAMENT, THE COUNCIL, THE EUROPEAN ECONOMIC AND SOCIAL COMMITTEE AND THE COMMITTEE OF THE REGIONS (COM/2020/299 Final)*; Brussels, 2020.

(10) Dunn, B.; Kamath, H.; Tarascon, J. M. *Electrical Energy Storage for the Grid: A Battery of Choices*; 2011; Vol. 334. https://doi.org/10.1126/science.1212741.

(11) Sagadevan, S.; Marlinda, A. R.; Chowdhury, Z. Z.; Wahab, Y. B. A.; Hamizi, N. A.; Shahid, M. M.; Mohammad, F.; Podder, J.; Johan, M. R. Fundamental Electrochemical Energy Storage Systems. In *Advances in Supercapacitor and Supercapattery*; Elsevier, 2021; pp 27–43. https://doi.org/10.1016/b978-0-12-819897-1.00001-x.

(12) Baumann, M.; Peters, J. F.; Weil, M.; Grunwald, A. CO2 Footprint and Life-Cycle Costs of Electrochemical Energy Storage for Stationary Grid Applications. *Energy Technol.* **2017**, *5* (7), 1071–1083. https://doi.org/10.1002/ente.201600622.

(13) Eurostat. Waste statistics - recycling of batteries and accumulators https://ec.europa.eu/eurostat/statistics-explained/index.php?title=Waste_statistics_-_recycling_of_batteries_and_accumulators&stable=0#Sales_and_collection_of_portable_batteries_and_accumulators (accessed May 25, 2021).

(14) BIO Intelligence. *Impact Assessment on Selected Policy Options for Revision of the Battery Directive*; 2003.

(15) ABRI (Australian Battery Recycling Initiative). Handheld Battery Recycling http://www.batteryrecycling.org.au/wp-content/uploads/2014/01/Handheld-battery-recycling-QA-2014.pdf (accessed Jun 5, 2021). https://doi.org/10.1002/9781118062111.part2.

(16) Rarotra, S.; Sahu, S.; Kumar, P.; Kim, K.-H.; Fai Tsang, Y.; Kumar, V.; Kumar, P.; Srinivasan, M.; Veksha, A.; Lisak, G. Progress and Challenges on Battery Waste Management :A Critical Review. **2020**. https://doi.org/10.1002/slct.202000618.

(17) Liu, C.; Lin, J.; Cao, H.; Zhang, Y.; Sun, Z. Recycling of Spent Lithium-Ion Batteries in View of Lithium Recovery: A Critical Review. *Journal of Cleaner Production*. Elsevier Ltd August 10, 2019, pp 801–813. https://doi.org/10.1016/j.jclepro.2019.04.304.

(18) Onianwa, P. C. *Informal Ulab Recycling in Africa: Case Studies of Selected Countries*; 2016.

(19) Schaddelee-Scholten, B.; Tempowski, J. *Recycling Used Lead-Acid Batteries: Health Considerations*; 2017.

(20) Larcher, D.; Tarascon, J. M. Towards Greener and More Sustainable Batteries for Electrical Energy Storage. *Nature Chemistry*. Nature Publishing Group January 1, 2015, pp 19–29. https://doi.org/10.1038/nchem.2085.

(21) Dühnen, S.; Betz, J.; Kolek, M.; Schmuch, R.; Winter, M.; Placke, T. Toward Green Battery Cells: Perspective on Materials and Technologies. *Small Methods*. John Wiley and Sons Inc. July 1, 2020, p 2000039. https://doi.org/10.1002/smtd.202000039.

(22) Ellingsen, L. A. W.; Holland, A.; Drillet, J. F.; Peters, W.; Eckert, M.; Concepcion, C.; Ruiz, O.; Colin, J. F.; Knipping, E.; Pan, Q.; Wills, R. G. A.; Majeau-Bettez, G. Environmental Screening of Electrode Materials for a Rechargeable Aluminum Battery with an AlCl3/EMIMCl Electrolyte. *Materials (Basel).* **2018**, *11* (6). https://doi.org/10.3390/ma11060936.

(23) Singh, R.; Polu, A. R.; Bhattacharya, B.; Rhee, H. W.; Varlikli, C.; Singh, P. K. Perspectives for Solid Biopolymer Electrolytes in Dye Sensitized Solar Cell and Battery Application. *Renewable and Sustainable Energy Reviews*. Elsevier Ltd November 1, 2016, pp 1098–1117. https://doi.org/10.1016/j.rser.2016.06.026.

(24) Sealy, C. The Problem with Platinum. *Materials Today*. Elsevier December 1, 2008, pp 65–68. https://doi.org/10.1016/S1369-7021(08)70254-2.

(25) Zhu, P.; Gastol, D.; Marshall, J.; Sommerville, R.; Goodship, V.; Kendrick, E. A Review of Current Collectors for Lithium-Ion Batteries. *Journal of Power Sources*. Elsevier B.V. February 15, 2021, p 229321. https://doi.org/10.1016/j.jpowsour.2020.229321.

(26) Dos Reis, G. S.; Larsson, S. H.; de Oliveira, H. P.; Thyrel, M.; Lima, E. C. Sustainable Biomass Activated Carbons as Electrodes for Battery and Supercapacitors–a Mini-Review. *Nanomaterials* **2020**, *10* (7), 1–22. https://doi.org/10.3390/nano10071398.

(27) Saleh Ahammad, A. J.; Lee, J. J.; Rahman, M. A. Electrochemical Sensors Based on Carbon Nanotubes. *Sensors*. Molecular Diversity Preservation International April 30, 2009, pp 2289–2319. https://doi.org/10.3390/s90402289.

(28) Brownson, D. A. C.; Banks, C. E. *The Handbook of Graphene Electrochemistry*; Springer: Manchester, 2014. https://doi.org/10.1007/978-1-4471-6428-9.

(29) Liang, J.; Mondal, A. K.; Wang, D. W.; Iacopi, F. Graphene-Based Planar Microsupercapacitors: Recent Advances and Future Challenges. *Advanced Materials Technologies*. Wiley-Blackwell January 1, 2019, p 1800200. https://doi.org/10.1002/admt.201800200.

(30) Ye, R.; James, D. K.; Tour, J. M. Laser-Induced Graphene: From Discovery to Translation. *Adv. Mater.* **2018**, *31* (1), 1803621. https://doi.org/10.1002/adma.201803621.

(31) Lin, J.; Peng, Z.; Liu, Y.; Ruiz-Zepeda, F.; Ye, R.; Samuel, E. L. G.; Yacaman, M. J.; Yakobson, B. I.; Tour, J. M. Laser-Induced Porous Graphene Films from Commercial Polymers. *Nat. Commun.* **2014**, *5* (1), 1–8. https://doi.org/10.1038/ncomms6714.

(32) Chyan, Y.; Ye, R.; Li, Y.; Singh, S. P.; Arnusch, C. J.; Tour, J. M. Laser-Induced Graphene by Multiple Lasing: Toward Electronics on Cloth, Paper, and Food. *ACS Nano* **2018**, *12* (3), 2176–2183. https://doi.org/10.1021/acsnano.7b08539.

(33) Ye, R.; Han, X.; Kosynkin, D. V.; Li, Y.; Zhang, C.; Jiang, B.; Martí, A. A.; Tour, J. M. Laser-Induced Conversion of Teflon into Fluorinated Nanodiamonds or Fluorinated Graphene. *ACS Nano* **2018**, *12* (2), 1083–1088. https://doi.org/10.1021/acsnano.7b05877.

(34) Xu, Y.; Fei, Q.; Page, M.; Zhao, G.; Ling, Y.; Chen, D.; Yan, Z. Laser-Induced Graphene for Bioelectronics and Soft Actuators. *Nano Research*. Tsinghua University April 7, 2021, pp 1–18. https://doi.org/10.1007/s12274-021-3441-9.

(35) Dong, Y.; Rismiller, S. C.; Lin, J. Molecular Dynamic Simulation of Layered Graphene Clusters Formation from Polyimides under Extreme Conditions. *Carbon N. Y.* **2016**, *104*, 47–55. https://doi.org/10.1016/j.carbon.2016.03.050.

(36) Chyan, Y.; Ye, R.; Li, Y.; Singh, S. P.; Arnusch, C. J.; Tour, J. M. Laser-Induced Graphene by Multiple Lasing: Toward Electronics on Cloth, Paper, and Food. *ACS Nano* **2018**, *12* (3), 2176–2183. https://doi.org/10.1021/acsnano.7b08539.

(37) Ye, R.; James, D. K.; Tour, J. M. Laser-Induced Graphene: From Discovery to Translation. *Advanced Materials*. Wiley-VCH Verlag January 4, 2019, p 1803621. https://doi.org/10.1002/adma.201803621.

(38) Chen, G.; Liu, Y.; Liu, F.; Zhang, X. Fabrication of Three-Dimensional Graphene Foam with High Electrical Conductivity and Large Adsorption Capability. *Appl. Surf. Sci.* **2014**, *311*, 808–815. https://doi.org/10.1016/j.apsusc.2014.05.171.

(39) Lee, S.; Jeon, S. Laser-Induced Graphitization of Cellulose Nanofiber Substrates under Ambient Conditions. *ACS Sustain. Chem. Eng.* **2019**, *7* (2), 2270–2275. https://doi.org/10.1021/acssuschemeng.8b04955.

(40) Ye, R.; Chyan, Y.; Zhang, J.; Li, Y.; Han, X.; Kittrell, C.; Tour, J. M. Laser-Induced Graphene Formation on Wood. *Adv. Mater.* **2017**, *29* (37). https://doi.org/10.1002/adma.201702211.

(41) Zhang, W.; Lei, Y.; Ming, F.; Jiang, Q.; Costa, P. M. F. J.; Alshareef, H. N. Lignin Laser Lithography: A Direct-Write Method for Fabricating 3D Graphene Electrodes for Microsupercapacitors. *Adv. Energy Mater.* **2018**, *8* (27), 1–9. https://doi.org/10.1002/aenm.201801840.

(42) Mahmood, F.; Zhang, C.; Xie, Y.; Stalla, D.; Lin, J.; Wan, C. Transforming Lignin into Porous Graphene via Direct Laser Writing for Solid-State Supercapacitors. *RSC Adv.* **2019**, *9* (39), 22713–22720. https://doi.org/10.1039/c9ra04073k.

(43) Edberg, J.; Brooke, R.; Hosseinaei, O.; Fall, A.; Wijeratne, K.; Sandberg, M. Laser-Induced Graphitization of a Forest-Based Ink for Use in Flexible and Printed Electronics. *npj Flex. Electron.* **2020**, *4* (1), 1–10. https://doi.org/10.1038/s41528-020-0080-2.

(44) Laplaza Arjona, M. Fabrication of Laser-Induced Graphene Structures on Paper and Cardboard for Sustainable Disposable Devices. *Treb. Final Grau, Univ. Autónoma Barcelona, Cerdanyola del Vallés* **2020**.

(45) Garcia Reig, J. Laser Induced Graphene. *Treb. Final Grau, Univ. Autónoma Barcelona, Cerdanyola del Vallés* **2019**.

(46) Zhang, Z.; Song, M.; Hao, J.; Wu, K.; Li, C.; Hu, C. Visible Light Laser-Induced Graphene from Phenolic Resin: A New Approach for Directly Writing Graphene-Based Electrochemical Devices on Various Substrates. *Carbon N. Y.* **2018**, *127*, 287–296. https://doi.org/10.1016/j.carbon.2017.11.014.

(47) Li, Y.; Luong, D. X.; Zhang, J.; Tarkunde, Y. R.; Kittrell, C.; Sargunaraj, F.; Ji, Y.; Arnusch, C. J.; Tour, J. M. Laser-Induced Graphene in Controlled Atmospheres: From Superhydrophilic to Superhydrophobic Surfaces. *Adv. Mater.* **2017**, *29* (27). https://doi.org/10.1002/adma.201700496.

(48) Peng, Z.; Ye, R.; Mann, J. A.; Zakhidov, D.; Li, Y.; Smalley, P. R.; Lin, J.; Tour, J. M. Flexible Boron-Doped Laser-Induced Graphene Microsupercapacitors. *ACS Nano* **2015**, *9* (6), 5868–5875. https://doi.org/10.1021/acsnano.5b00436.

(49) Li, L.; Zhang, J.; Peng, Z.; Li, Y.; Gao, C.; Ji, Y.; Ye, R.; Kim, N. D.; Zhong, Q.; Yang, Y.; Fei, H.; Ruan, G.; Tour, J. M. High-Performance Pseudocapacitive Microsupercapacitors from Laser-Induced Graphene. *Adv. Mater.* **2016**, *28* (5), 838–845. https://doi.org/10.1002/adma.201503333.

(50) Bobinger, M. R.; Romero, F. J.; Salinas-Castillo, A.; Becherer, M.; Lugli, P.; Morales, D. P.; Rodríguez, N.; Rivadeneyra, A. Flexible and Robust Laser-Induced Graphene Heaters Photothermally Scribed on Bare Polyimide Substrates. *Carbon N. Y.* **2019**, *144*, 116–126. https://doi.org/10.1016/j.carbon.2018.12.010.

(51) Ye, R.; Chyan, Y.; Zhang, J.; Li, Y.; Han, X.; Kittrell, C.; Tour, J. M. Laser-Induced Graphene Formation on Wood. *Adv. Mater.* **2017**, *29* (37), 1702211. https://doi.org/10.1002/adma.201702211.

(52) Tehrani, F.; Beltrán-Gastélum, M.; Sheth, K.; Karajic, A.; Yin, L.; Kumar, R.; Soto, F.; Kim, J.; Wang, J.; Barton, S.; Mueller, M.; Wang, J. Laser-Induced Graphene Composites for Printed, Stretchable, and Wearable Electronics. *Adv. Mater. Technol.* **2019**, *4* (8), 1900162. https://doi.org/10.1002/admt.201900162.

(53) Tiliakos, A.; Ceaus, C.; Iordache, S. M.; Vasile, E.; Stamatin, I. Morphic Transitions of Nanocarbons via Laser Pyrolysis of Polyimide Films. *J. Anal. Appl. Pyrolysis* **2016**, *121*, 275–286. https://doi.org/10.1016/j.jaap.2016.08.007.

(54) Tan, K. W.; Jung, B.; Werner, J. G.; Rhoades, E. R.; Thompson, M. O.; Wiesner, U. Transient Laser Heating Induced Hierarchical Porous Structures from Block Copolymer-Directed Self-Assembly. *Science (80-.).* **2015**, *349* (6243), 54–58. https://doi.org/10.1126/science.aab0492.

(55) Khan, M. A.; Hristovski, I. R.; Marinaro, G.; Kosel, J. Magnetic Composite Hydrodynamic Pump with Laser-Induced Graphene Electrodes. *IEEE Trans. Magn.* **2017**, *53* (11). https://doi.org/10.1109/TMAG.2017.2707598.

(56) Tao, L. Q.; Tian, H.; Liu, Y.; Ju, Z. Y.; Pang, Y.; Chen, Y. Q.; Wang, D. Y.; Tian, X. G.; Yan, J. C.; Deng, N. Q.; Yang, Y.; Ren, T. L. An Intelligent Artificial Throat with Sound-Sensing Ability Based on Laser Induced Graphene. *Nat. Commun.* **2017**, *8*. https://doi.org/10.1038/ncomms14579.

(57) Hayashi, S.; Nakajima, Y.; Terakawa, M. Strain Sensing Using Electrically Conductive Structures Fabricated by Femtosecond-Laser-Based Modification of PDMS. *Opt. Mater. Express* **2019**, *9* (6), 2672. https://doi.org/10.1364/ome.9.002672.

(58) Cheng, C.; Wang, S.; Wu, J.; Yu, Y.; Li, R.; Eda, S.; Chen, J.; Feng, G.; Lawrie, B.; Hu, A. Bisphenol A Sensors on Polyimide Fabricated by Laser Direct Writing for Onsite River Water Monitoring at Attomolar Concentration. *ACS Appl. Mater. Interfaces* **2016**, *8* (28), 17784–17792. https://doi.org/10.1021/acsami.6b03743.

(59) Zhang, C.; Xie, Y.; Deng, H.; Tumlin, T.; Zhang, C.; Su, J. W.; Yu, P.; Lin, J. Monolithic and Flexible ZnS/SnO2 Ultraviolet Photodetectors with Lateral Graphene Electrodes. *Small* **2017**, *13* (18), 1604197–1604198. https://doi.org/10.1002/smll.201604197.

(60) Ma, W.; Zhu, J.; Wang, Z.; Song, W.; Cao, G. Recent Advances in Preparation and Application of Laser-Induced Graphene in Energy Storage Devices. *Materials Today Energy*. Elsevier Ltd December 1, 2020, p 100569. https://doi.org/10.1016/j.mtener.2020.100569.

(61) Tiliakos, A.; Trefilov, A. M. I.; Tanasă, E.; Balan, A.; Stamatin, I. Laser-Induced Graphene as the Microporous Layer in Proton Exchange Membrane Fuel Cells. *Appl. Surf. Sci.* **2020**, *504*, 144096. https://doi.org/10.1016/j.apsusc.2019.144096.

(62) Yi, J.; Chen, J.; Yang, Z.; Dai, Y.; Li, W.; Cui, J.; Ciucci, F.; Lu, Z.; Yang, C. Facile Patterning of Laser-Induced Graphene with Tailored Li Nucleation Kinetics for Stable Lithium-Metal Batteries. *Adv. Energy Mater.* **2019**, *9* (38), 1901796. https://doi.org/10.1002/aenm.201901796.

(63) Ren, M.; Zhang, J.; Tour, J. M. Laser-Induced Graphene Hybrid Catalysts for Rechargeable Zn-Air Batteries. *ACS Appl. Energy Mater.* **2019**, *2* (2), 1460–1468. https://doi.org/10.1021/acsaem.8b02011.

(64) Ren, M.; Zhang, J.; Fan, M.; Ajayan, P. M.; Tour, J. M. Li-Breathing Air Batteries Catalyzed by MnNiFe/Laser-Induced Graphene Catalysts. *Adv. Mater. Interfaces* **2019**, *6* (19), 1901035. https://doi.org/10.1002/admi.201901035.

(65) Ren, M.; Zhang, J.; Zhang, C.; Stanford, M. G.; Chyan, Y.; Yao, Y.; Tour, J. M. Quasi-Solid-State Li-O2 Batteries with Laser-Induced Graphene Cathode Catalysts. *ACS Appl. Energy Mater.* **2020**, *3* (2), 1702–1709. https://doi.org/10.1021/acsaem.9b02182.

(66) Esquivel, J. P.; Alday, P.; Ibrahim, O. A.; Fernández, B.; Kjeang, E.; Sabaté, N. A Metal-Free and Biotically Degradable Battery for Portable Single-Use Applications. *Adv. Energy Mater.* **2017**, *7* (18), 1700275. https://doi.org/10.1002/aenm.201700275.

(67) Merino-Jimenez, I.; Llorella, A.; Navarro-Segarra, M.; Agramunt, J.; Grandas, A.; Minteer, S. D.; Esquivel, J. P.; Sabaté, N. A Self-Powered Minimalistic Glucometer: A Lean Approach to Sustainable Single-Use Point-of-Care Devices. *Adv. Mater. Technol.* **2021**, *6* (5), 2001051. https://doi.org/10.1002/admt.202001051.

(68) Ortega, L.; Llorella, A.; Esquivel, J. P.; Sabaté, N. Self-Powered Smart Patch for Sweat Conductivity Monitoring. *Microsystems Nanoeng.* **2019**, *5* (1). https://doi.org/10.1038/s41378-018-0043-0.

(69) van der Pauw, L. J. A Method of Measuring Specific Resistivity and Hall Effect of Discs of Arbitrary Shape. In *Semiconductor Devices: Pioneering Papers*; WORLD SCIENTIFIC, 1991; pp 174–182. https://doi.org/10.1142/9789814503464_0017.

(70) Keysight. Sheet Resistivity and Sheet Resistance Measurement Using an SMU | Application Note https://www.keysight.com/es/en/assets/7018-05102/application-notes/5992-1329.pdf (accessed Jun 3, 2021).

(71) Elgrishi, N.; Rountree, K. J.; McCarthy, B. D.; Rountree, E. S.; Eisenhart, T. T.; Dempsey, J. L. A Practical Beginner's Guide to Cyclic Voltammetry. *J. Chem. Educ.* **2018**, *95* (2), 197–206. https://doi.org/10.1021/acs.jchemed.7b00361.

(72) Randles, J. E. B. A Cathode Ray Polarograph. Part II. - The Current-Voltage Curves. *Trans. Faraday Soc.* **1948**, *44* (0), 327–338. https://doi.org/10.1039/TF9484400327.

(73) Ševčík, A. Oscillographic Polarography with Periodical Triangular Voltage. *Collect. Czechoslov. Chem. Commun.* **1948**, *13*, 349–377. https://doi.org/10.1135/cccc19480349.

(74) Nicholson, R. S. Theory and Application of Cyclic Voltammetry for Measurement of Electrode Reaction Kinetics. *Anal. Chem.* **1965**, *37* (11), 1351–1355. https://doi.org/10.1021/ac60230a016.

(75) Lavagnini, I.; Antiochia, R.; Magno, F. An Extended Method for the Practical Evaluation of the Standard Rate Constant from Cyclic Voltammetric Data. *Electroanalysis* **2004**, *16* (6), 505–506. https://doi.org/10.1002/elan.200302851.

(76) Klingler, R. J.; Kochi, J. K. Electron-Transfer Kinetics from Cyclic Voltammetry. Quantitative Description of Electrochemical Reversibility. *J. Phys. Chem.* **1981**, *85* (12), 1731–1741. https://doi.org/10.1021/j150612a028.

(77) Yi, F.; Ren, H.; Shan, J.; Sun, X.; Wei, D.; Liu, Z. Wearable Energy Sources Based on 2D Materials. *Chemical Society Reviews*. Royal Society of Chemistry May 7, 2018, pp 3152–3188. https://doi.org/10.1039/c7cs00849j.

(78) Yang, P.; Mai, W. Flexible Solid-State Electrochemical Supercapacitors. *Nano Energy*. Elsevier Ltd September 1, 2014, pp 274–290. https://doi.org/10.1016/j.nanoen.2014.05.022.

(79) Ratha, S.; Samantara, A. K. Characterization and Performance Evaluation of Supercapacitor; Springer, Singapore, 2018; pp 23–43. https://doi.org/10.1007/978-981-13-3086-5_3.

(80) Jonscher, A. K. Charging and Discharging of Non-Ideal Capacitors. *IEEE Trans. Electr. Insul.* **1987**, *EI-22* (4), 357–359. https://doi.org/10.1109/TEI.1987.298893.

(81) Laheäär, A.; Przygocki, P.; Abbas, Q.; Béguin, F. Appropriate Methods for Evaluating the Efficiency and Capacitive Behavior of Different Types of Supercapacitors. *Electrochem. commun.* **2015**, *60*, 21–25. https://doi.org/10.1016/j.elecom.2015.07.022.

(82) Mathis, T. S.; Kurra, N.; Wang, X.; Pinto, D.; Simon, P.; Gogotsi, Y. Energy Storage Data Reporting in Perspective—Guidelines for Interpreting the Performance of Electrochemical Energy Storage Systems. *Advanced Energy Materials*. Wiley-VCH Verlag October 1, 2019, p 1902007. https://doi.org/10.1002/aenm.201902007.

(83) Winter, M.; Brodd, R. J. What Are Batteries, Fuel Cells, and Supercapacitors? *Chem. Rev.* **2004**, *104* (10), 4245–4269. https://doi.org/10.1021/cr020730k.

(84) Aaron, D.; Tang, Z.; Papandrew, A. B.; Zawodzinski, T. A. Polarization Curve Analysis of All-Vanadium Redox Flow Batteries. *J. Appl. Electrochem.* **2011**, *41* (10), 1175–1182. https://doi.org/10.1007/s10800-011-0335-7.

(85) Eurostat. Packaging waste statistics - Statistics Explained https://ec.europa.eu/eurostat/statistics-explained/index.php/Packaging_waste_statistics (accessed May 31, 2021).

(86) Packaging Europe. Paper and cardboard recycling reach record high across Europe https://packagingeurope.com/paper-and-cardboard-recycling-have-reached-record-high-acros/ (accessed May 31, 2021).

(87) Zhou, W.; Gong, Z.; Zhang, L.; Liu, Y.; Yan, J.; Zhao, M. Feasibility of Lipid Production from Waste Paper by the Oleaginous Yeast Cryptococcus Curvatus. *BioResources* **2017**, *12* (3), 5249–5263. https://doi.org/10.15376/biores.12.3.5249-5263.

(88) Leipa Georg Leinfelder GMBH. Manilla-RCK STANDARD-PRODUKT-SPEZIFIKATION https://www.burgodistribuzione.com/sites/default/files/schede_tecniche/manilla.pdf (accessed Jun 8, 2021).

(89) EpilogLaser. *MINI 18/24 & HELIX Laser System Manual | Model 8000*; 2020.

(90) Mikheev, K. G.; Zonov, R. G.; Mogileva, T. N.; Fateev, A. E.; Mikheev, G. M. Optical Anisotropy of Laser-Induced Graphene Films. *Opt. Laser Technol.* **2021**, *141*, 107143. https://doi.org/10.1016/j.optlastec.2021.107143.

(91) Thess, A.; Lee, R.; Nikolaev, P.; Dai, H.; Petit, P.; Robert, J.; Xu, C.; Lee, Y. H.; Kim, S. G.; Rinzler, A. G.; Colbert, D. T.; Scuseria, G. E.; Tománek, D.; Fischer, J. E.; Smalley, R. E. Crystalline Ropes of Metallic Carbon Nanotubes. *Science (80-.).* **1996**, *273* (5274), 483–487. https://doi.org/10.1126/science.273.5274.483.

(92) Lee, G.; Kang, S. K.; Won, S. M.; Gutruf, P.; Jeong, Y. R.; Koo, J.; Lee, S. S.; Rogers, J. A.; Ha, J. S. Fully Biodegradable Microsupercapacitor for Power Storage in Transient Electronics. *Adv. Energy Mater.* **2017**, *7* (18), 1700157. https://doi.org/10.1002/aenm.201700157.

ANNEX I: Power variation in laser stage

Figure 24. *Cardboard rastered with the same lasing parameters at different positions of the sample stage. a) With extractor switched on, and b) with extractor switched off (scalebar for sample stage, 90 mm; charred squares in insight pictures are 4x4 mm^2 sized).*

ANNEX II: Laser spot distance and diameter with defocus

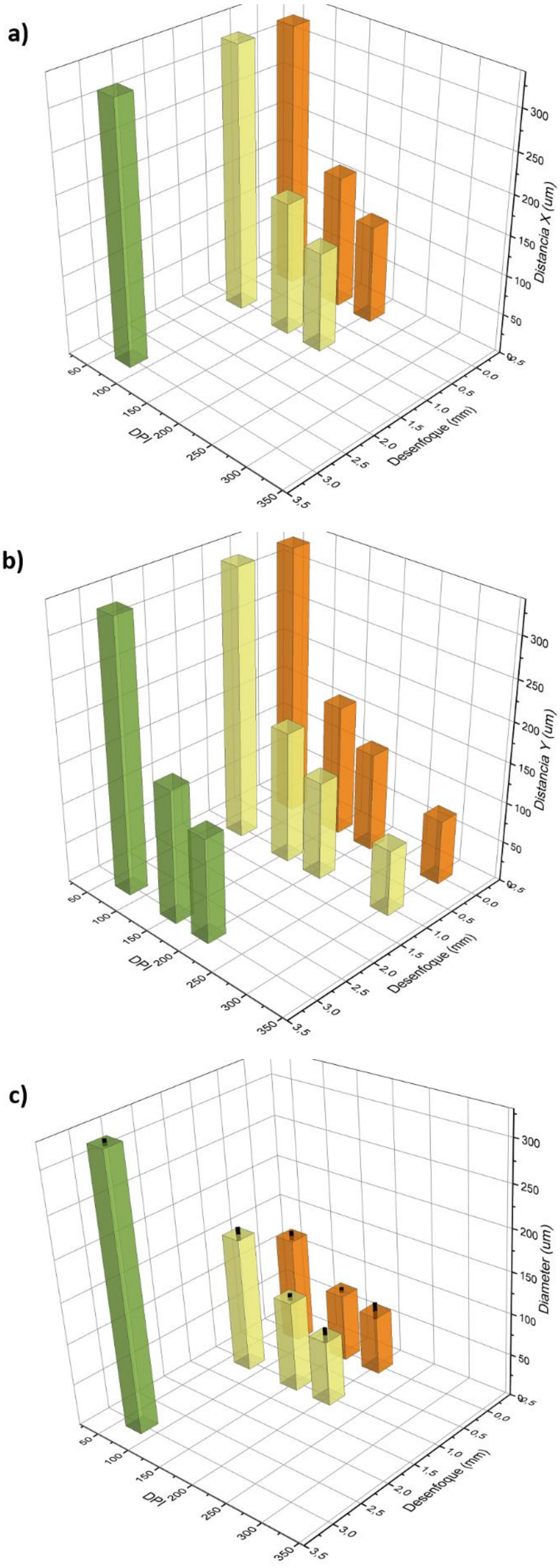

Figure 25. *Variation of lased spot separation with DPI resolution and defocus. a) In X axis. b) In Y axis. c) Variation of lased spot diameter with DPI resolution and defocus.*

ANNEX III: CVs performed in LIGNIN+NC_LIG

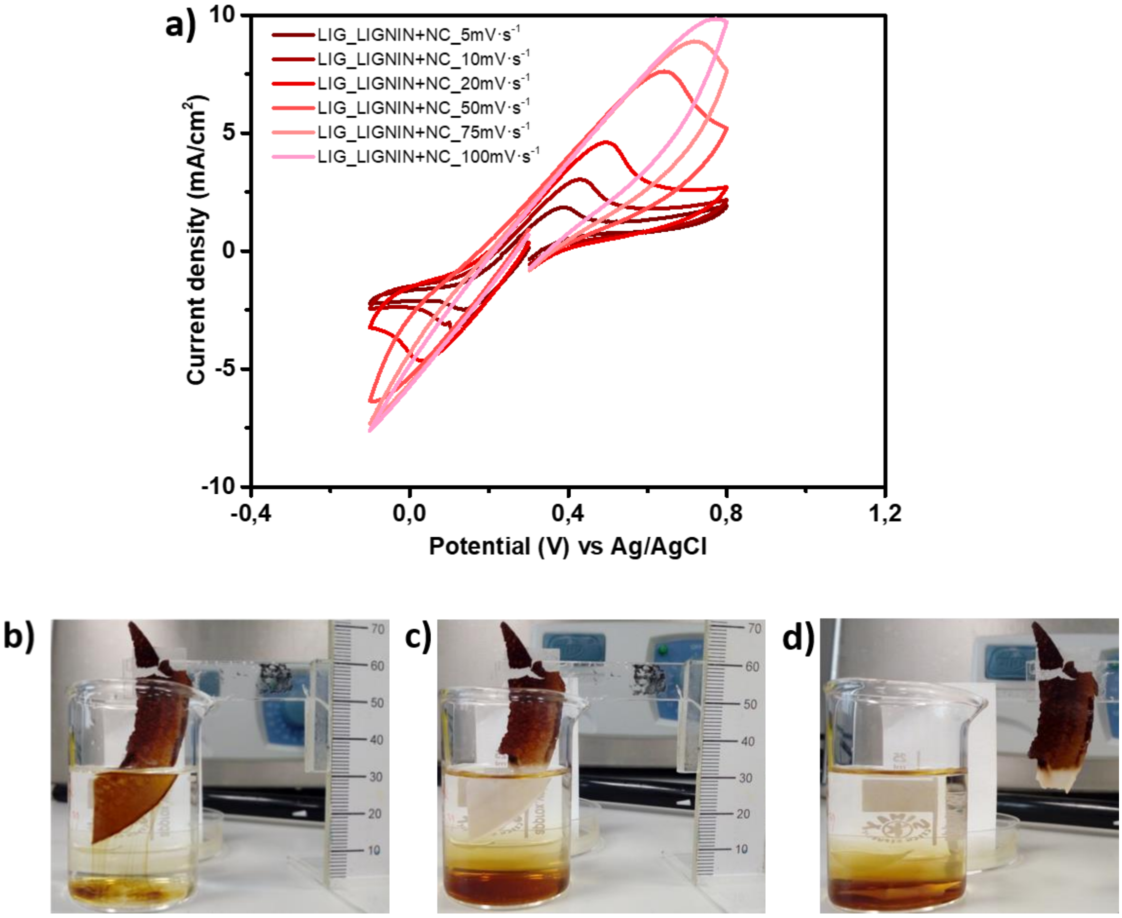

Figure 26. *a) CVs performed in LIGNIN+NC_LIG electrodes with varying scan rate with 100 mM ferricyanide and 1M KCl. LIGNIN+NC membrane mechanical destabilization in DI water. b) Seconds after immersion. c) One hour after immersion. d) After removing membrane from water it broke.*

As shown in Figure 24a, it has been possible to perform CV experiments in LIGNIN+NC_LIG electrodes. However, the mechanical instability of the coating of lignin and nanocellulose in water has complicated its measurement, as part of the lignin has dissolved into the ferricyanide solution contaminating it. Moreover, the coating has demonstrated to be instable in water, as lignin dissolves and the remaining nanocellulose membrane losses its mechanical properties.

ANNEX IV: Compensation of design dimensions

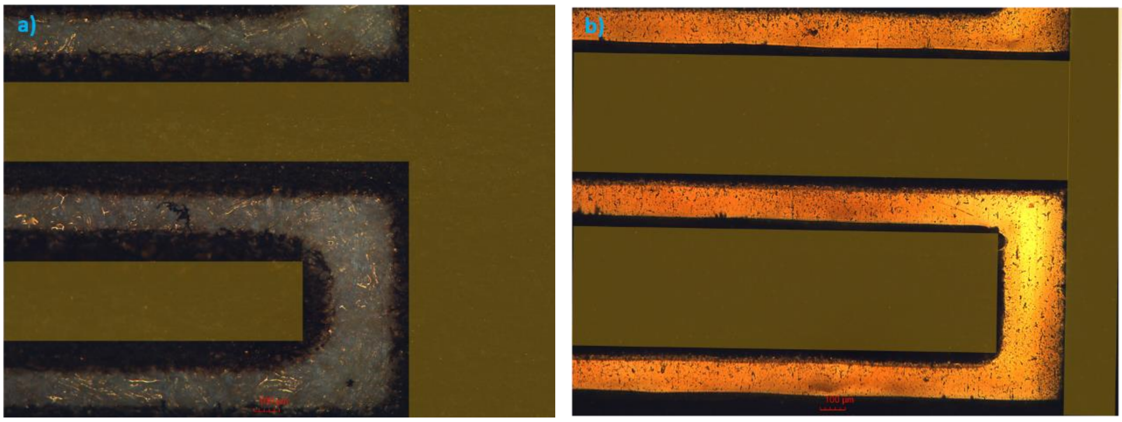

Figure 27. *a) Optical microscope image of interdigitated electrodes of FRS_SC with Corel design superimposed in yellow. d) Optical microscope image of interdigitated electrodes of PI_SC with Corel design superimposed in yellow.*

As laser spot size has a finite diameter that changes with defocusing, different CorelDRAW designs have been created to scribe SCs on FRS treated cardboard 3 mm defocused and on PI focused. The final interdigitated electrodes are 5130 µm long, 550 µm wide, separated by 150 µm from one another and 220 µm from the other electrodes' contact pad.

ANNEX V: Lignin coating treatments

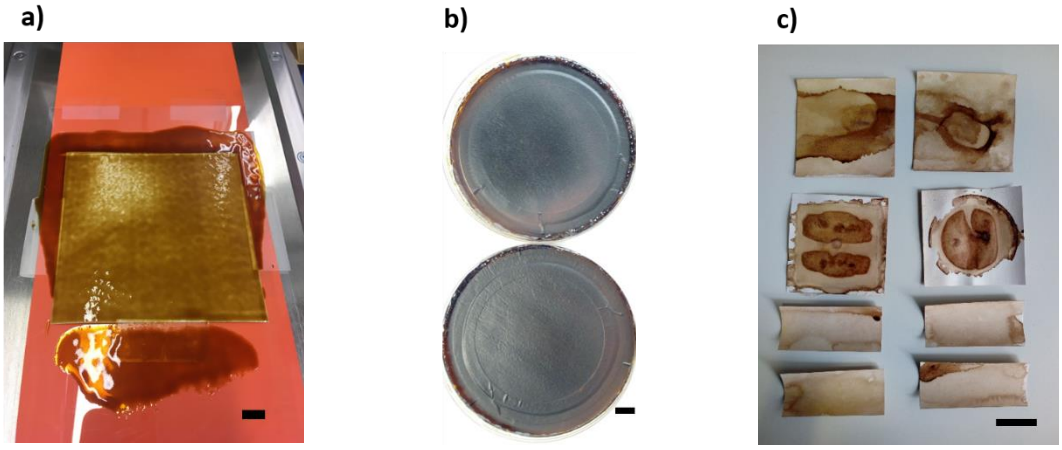

Figure 28. *Different lignin treatments tested on cardboard a) Bar coating of hydrogel (scalebar, 1 cm). b) Water evaporation of hydrogel on Petri dish (scalebar, 1 cm). c) Lignin aqueous solution spraying (scalebar, 4 cm).*

ANNEX VI: CVs performed with 100 mM ferricyanide

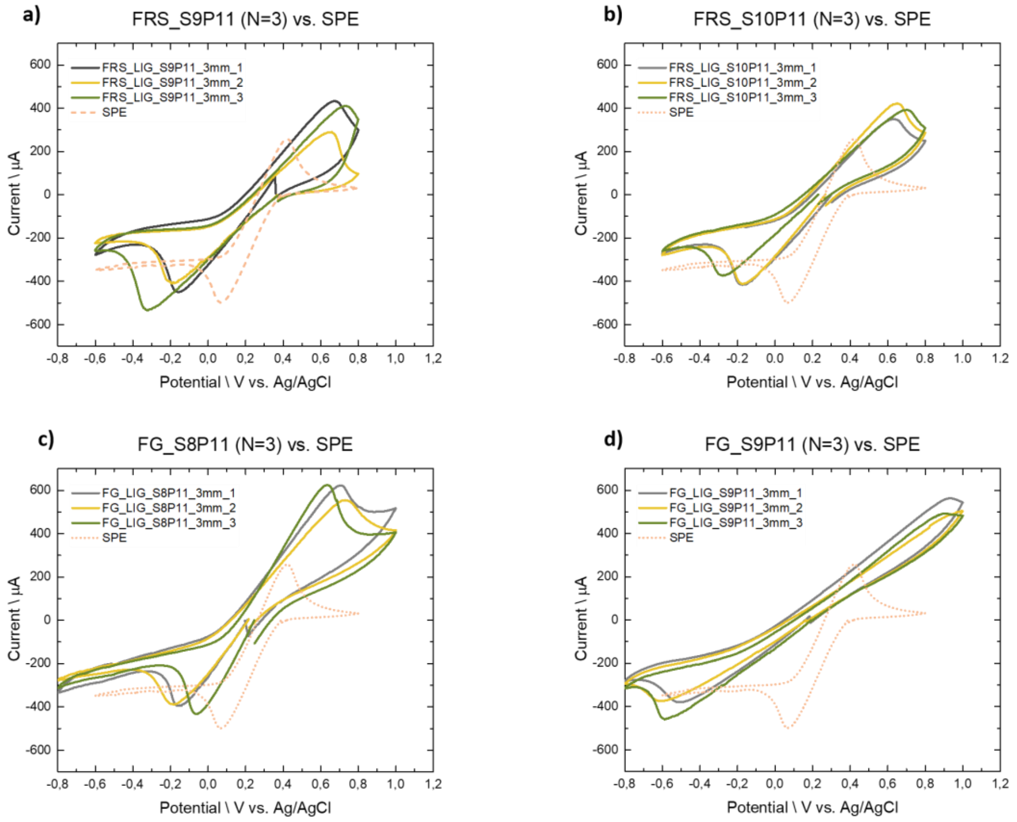

Figure 29. *CVs performed with fire-retardant treated cardboard derived LIG electrodes vs SPE, in 100 mM ferricyanide 1 M KCl solution, with a commercial Ag/AgCl reference electrode and a Pt counter electrode, at 20 mV·s^{-1} scan rate. a) FRS_LIG_S9P11_3mm electrodes. b) FRS_LIG_S10P11_3mm electrodes. c) FG_LIG_S8P11_3mm electrodes. d) FG_LIG_S9P11_3mm electrodes.*

ANNEX VII: Fabrication challenges of LIG on FG treated cardboard

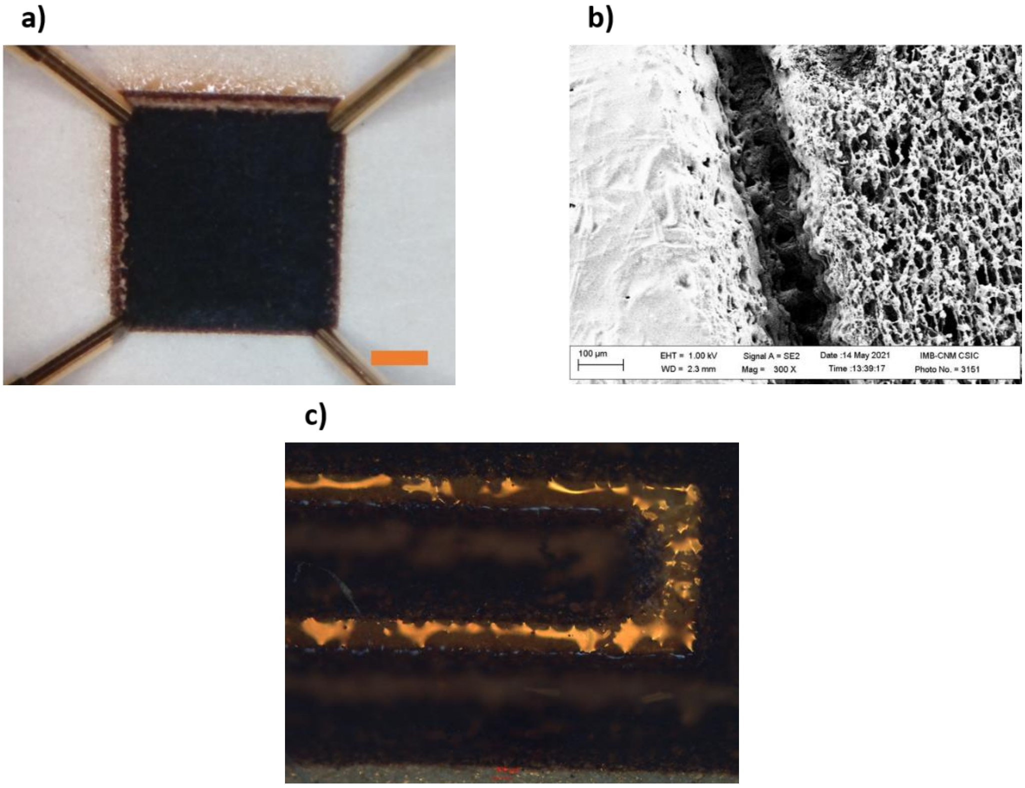

Figure 30. *Microscope images showing trench in the border of scribed FG treated cardboard, disabling it for interdigitated electrode fabrication. a) 4x4 mm*^{2} *square of FG_LIG_S8P11_3mm in the four-point probe station (scalebar, 1 mm). b) Scanning electron microscope image (1 kV) of 4x4 mm*^{2} *square border, showing a deep trench. c) Optical microscope image of interdigitated electrodes fabricated with FG_LIG, showing structures with several defects and very narrow LIG conductor path.*